

# MOLECULAR LINE OBSERVATIONS OF INFRARED DARK CLOUDS: SEEKING THE PRECURSORS TO INTERMEDIATE AND MASSIVE STAR FORMATION

S. E. RAGAN<sup>1</sup>, E. A. BERGIN<sup>1</sup>, R. PLUME<sup>2</sup>, D. L. GIBSON<sup>2</sup>, D. J. WILNER<sup>3</sup>, S. O'BRIEN<sup>4</sup> & E. HAILS<sup>5</sup>

*Draft version September 23, 2018*

## ABSTRACT

We have identified 41 infrared dark clouds from the 8  $\mu\text{m}$  maps of the Midcourse Space Experiment (MSX), selected to be found within one square degree areas centered on known ultracompact HII regions. We have mapped these infrared dark clouds in  $\text{N}_2\text{H}^+$   $1 \rightarrow 0$ , CS  $2 \rightarrow 1$  and  $\text{C}^{18}\text{O}$   $1 \rightarrow 0$  emission using the Five College Radio Astronomy Observatory. The maps of the different species often show striking differences in morphologies, indicating differences in evolutionary state and/or the presence of undetected, deeply embedded protostars. We derive an average mass for these clouds using  $\text{N}_2\text{H}^+$  column densities of  $\approx 2500 \text{ M}_\odot$ , a value comparable to that found in previous studies of high mass star forming cores using other mass tracers. The linewidths of these clouds are typically  $\sim 2.0 - 2.9 \text{ km s}^{-1}$ . Based on the fact that they are dark at 8  $\mu\text{m}$ , compact, massive, and have large velocity dispersions, we suggest that these clouds may be the precursor sites of intermediate and high mass star formation.

*Subject headings:* ISM: clouds — ISM: molecules — stars: formation

## 1. INTRODUCTION

The study of star formation has made tremendous strides over the past two decades. Advances in observational capabilities have allowed a number of phases of the star formation process to be identified and characterized, starting with the centrally concentrated core of molecular gas that collapses to form a star surrounded by a proto-planetary disk. It has been the isolation of such objects that have not yet formed stars – pre-stellar cores – that has allowed us to probe the earliest initial stages of star formation (see André et al. 2000; Alves, Lada & Lada 2000). Most of the progress has focused on the formation of low-mass stars, predominantly because these objects can form isolated from other nearby stars that reduces confusion, and, conveniently, there is a large sample of such objects located in nearby clouds. However, it has now been recognized that most stars that are more massive than the Sun do not form in isolated fashion, but rather in clusters of  $>100$  stars (Zinnecker et al. 1993).

Progress in our understanding of high-mass star formation has been hampered by a number of factors: (1) timescales for massive star formation are short and examples in a given state are intrinsically rare, (2) the large distances to the Giant Molecular Clouds (GMCs) that are the birth sites of massive stars make studies of individual objects difficult, and (3) the very nature of clustered star formation increases confusion (cf. Garay & Lizano 1999). As a result, the objects in the earliest phases – the “pre-stellar massive cores” – have been difficult to identify.

The traditional method of locating low-mass cores has been to examine optical plates for regions of obscured starlight and then to pursue follow up molecular line observations (Myers & Benson 1983; Lee & Myers 1999). A comparison with the IRAS point source catalog then denotes whether these cores are associated with newly formed stars (Beichmann et al. 1986). This method cannot be applied to massive star forming regions since the greater distances makes isolating individual objects difficult. Moreover, the size and high column densities of GMCs makes it impossible to use optical plates to find individual objects. An analogous method of searching for molecular cores is to search for obscured regions in galactic mid-infrared background. However, due to atmospheric constraints, ground-based observations in the mid-IR are difficult to obtain. The ISOCAM instrument on the Infrared Space Observatory was used in this fashion, but only with pointed observations towards previously identified cores (e.g. Bacmann et al. 2000).

The Midcourse Space Experiment (MSX) surveyed the galactic plane in mid-infrared bands spanning from 7 to 25  $\mu\text{m}$ . This survey revealed a large population of dark clouds, predominantly located toward the inner galaxy (Egan et al. 1998). Follow-up molecular studies of a few objects confirmed that the obscured regions represent a new population of dense,  $n(\text{H}_2) > 10^5 \text{ cm}^{-3}$ , and cold,  $T < 20 \text{ K}$ , molecular clouds (Carey et al 1998). Further comparison to IRAS images demonstrated that most of these clouds are dark from 7–100  $\mu\text{m}$ , presumably because these objects either do not contain newly formed stars, or any newly formed stars are very deeply embedded. As such, a sub-sample of these objects may trace massive pre-stellar cores. There has been substantial activity in this field recently, with numerous groups analyzing various samples of infrared dark clouds (IRDCs). These studies have shown that it is likely that IRDCs are the birth-sites of high-mass stars and stellar clusters (Sridharan et al. 2005, Menten et al. 2005, Rathborne et al. 2006, Pillai et al. 2006).

We have identified a sample of infrared dark clouds and

<sup>1</sup> Dept. of Astronomy, University of Michigan, Ann Arbor, MI, USA

<sup>2</sup> Dept. of Physics and Astronomy, University of Calgary, Calgary, AB, Canada

<sup>3</sup> Harvard-Smithsonian Center for Astrophysics, Cambridge, MA, USA

<sup>4</sup> Dept. of Physics, University of Notre Dame, Notre Dame, IN, USA

<sup>5</sup> Arizona Radio Observatory, Tucson, AZ, USA

searched them for emission from the  $\text{N}_2\text{H}^+ 1 \rightarrow 0$ , CS  $2 \rightarrow 1$  and  $\text{C}^{18}\text{O } 1 \rightarrow 0$  transitions (§2). In most cases, we find that the emission closely corresponds to the MSX dark regions. Using a gas temperature of  $T=15$  K based on CO  $1 \rightarrow 0$  data, we deduce several properties of the dark clouds including column density and mass (§3). We summarize our findings and the implications (§4).

## 2. SOURCE SELECTION & OBSERVATIONS

To search for pre-stellar massive cores we have compiled a catalog of MSX dark clouds. This catalog is biased, as we have only searched the released MSX band A (centered at  $8.8 \mu\text{m}$ ) images for infrared dark clouds in the vicinity of known ultra-compact (UC) HII regions from the Wood & Churchwell (1989) catalog. More specifically, we searched for absorbing clouds within a square degree centered on a given UC HII region. This strategy takes advantage of the fact that young stars generally form in clusters, and, therefore, a good place to search for the pre-cursors to massive stars is in the vicinity of regions with current massive star formation evidenced by the UC HII regions. In this fashion we have isolated 114 infrared dark clouds, of which only a small fraction (15%) have known associations with radio sources or masers. From this catalog of 114 infrared dark clouds we selected a sub-sample of the 41 most compact and most opaque ( $\tau_{8.8\mu\text{m}} \gtrsim 0.4$ ) cores and targeted these for molecular line observations.

We mapped 41 of the sample of MSX dark clouds in emission from  $\text{C}^{18}\text{O } J = 1 \rightarrow 0$  ( $\nu = 109.782$  GHz), CS  $J = 2 \rightarrow 1$  ( $\nu = 97.981$  GHz), and  $\text{N}_2\text{H}^+ J = 1 \rightarrow 0$  ( $\nu = 93.173$  GHz) using the 14m Five College Radio Astronomy Observatory (FCRAO). The observations were made in 2002 February, May & December using the 16 element focal plane array receiver SEQUOIA. Each  $2.5' \times 2.5'$  region was mapped with the  $50''$  beam, with typical rms noise levels of  $\sim 0.05 - 0.1$  K. We used the Narrow Band Correlator backend configured to a velocity resolution of  $\sim 0.13$  km s $^{-1}$ . Typical system temperatures ( $T_{\text{sys}}$ ) were 200 – 300 K. Main beam efficiencies ( $\eta_{\text{mb}}$ ) were approximated at 50% from the standard FCRAO values. This is accurate within a few percent for each transition. For each spectrum, a first-order, linear baseline was fit to remove instrumental and continuum offsets and drift.

This selection of species is motivated by studies of low-mass pre-stellar clouds.  $\text{N}_2\text{H}^+$  is unlikely to significantly suffer from the effects of depletion as the core condenses, and this species is a good tracer of the dense centers of starless cores (Bergin & Langer 1997; Tafalla et al. 2002). Conversely,  $\text{C}^{18}\text{O}$  and CS emission can be used to trace the outer layers. Table 1 lists some basic dark cloud properties such as the HII region name, the coordinates, the size, and the center-to-edge brightness contrast. The brightness contrast was obtained by comparing the brightness in the band centered at  $8.8 \mu\text{m}$  at the center of the core with the average background brightness, estimated from an average of the intensities in a vertical and horizontal slit across the dark region. If the dark cloud was searched for molecular emission, we provide the LSR velocity range to which the observations were sensitive.

In an appendix, we provide a source by source description of any associations with known star formation in-

dicators (e.g. IRAS sources, masers, radio continuum sources). The large majority of our sources have no association with any known strong infrared source.

## 3. RESULTS

### 3.1. Molecular Line Fits

Each line is fit with a Gaussian profile to determine the integrated intensity, line width, and the LSR velocity of the emitting material. Table 2 presents the results of the spectral line fitting. All parameters were extracted by standard Gaussian fitting methods in the CLASS package (Buisson et al. 2002); for  $\text{N}_2\text{H}^+$ , the seven hyperfine components were fit together using the HFS routine. The reported line-center velocity corresponds to that of the strongest hyperfine component ( $J = 1 \rightarrow 0$ ,  $F_1, F = 2, 3 \rightarrow 1, 2$ ) at 93.1738 GHz.

Our observations were obtained with velocity resolution of 0.13 km s $^{-1}$ , and to increase the signal to noise, we on occasion smoothed the line profiles by a factor of 2. As such, we had little sensitivity to structure within the line. Within our sensitivity limits (see §2), we see no evidence for extended line wings, and all lines were well-fit by single Gaussians. We report here only basic line properties.

### 3.2. Molecular Emission Morphologies

Figure 1 displays the Midcourse Space Experiment (MSX) images of each dark cloud overlaid with the integrated intensity maps of molecular emission for all observed molecular transitions. The contour levels for each dark cloud are specified in the captions. In some cases, multiple velocity components are detected, and the different velocity components are given different colors. The blue contours always correspond to the molecular emission morphology that most closely corresponds to the distribution of  $8 \mu\text{m}$  absorption seen in the MSX image, and, therefore, is most likely to be associated with the dark cloud. The line properties of the other velocity components (i.e. emission that is unassociated with the absorbing cloud) are not reported. There are three cases in which an a/b designation was assigned to distinguish two emission peaks. For G14.33-0.57 and G23.48-0.53, there are two spatially distinct and separate emission peaks at approximately the same characteristic velocity. This may suggest that in these cases, we were able to resolve spatially separated fragments of a cloud. In the case of G37.44+0.14, there are two velocity components that appear to correspond to absorbing regions (the 40 km s $^{-1}$  feature corresponding to the central absorbing cloud; the 18 km s $^{-1}$  feature corresponding to absorption to the north and west). Based on our assumptions, this would indicate that there are two unassociated dark clouds apparent in the same region of the sky by chance.

The morphological differences seen in Figure 1 are striking. Some maps show well defined cores in all three molecular tracers (e.g. G32.01+0.05). Other maps, like G06.26-0.51, show fairly well defined cores in  $\text{C}^{18}\text{O}$  and CS, but nothing obvious is seen in the  $\text{N}_2\text{H}^+$ . And others, like G09.21-0.22, show a strong centrally concentrated  $\text{N}_2\text{H}^+$  core but CS that is much more diffuse. Finally, there are cores like G10.59-0.31 that show no real evidence for molecular emission centered on the dark cloud at all. In this case, it is possible that any molecular emis-

sion directly associated with the dark cloud lies outside of the observed velocity band (see Table 1).

These differences in the molecular emission maps may be the result of differences in the evolutionary states. It is well known that CS and  $\text{C}^{18}\text{O}$  can form relatively quickly in the gas phase whereas  $\text{N}_2\text{H}^+$  takes significantly longer. However, as density enhances, the CS and  $\text{C}^{18}\text{O}$  tend to deplete onto the surfaces of dust grains, whereas  $\text{N}_2\text{H}^+$  will remain in the gas phase. Upon protostar formation, CS and  $\text{C}^{18}\text{O}$  can be released from dust grain surfaces (e.g. see models of Bergin & Langer 1997; Lee et al. 2004). Therefore, two scenarios can lead to the low abundance of  $\text{N}_2\text{H}^+$  relative to CS or  $\text{C}^{18}\text{O}$ : the star forming core is at an early stage of condensation and the densities are low such that CS and  $\text{C}^{18}\text{O}$  would be not affected by dust depletion, or the presence of a protostar has released the CS and  $\text{C}^{18}\text{O}$  from dust grains, all the while the  $\text{N}_2\text{H}^+$  abundance is essentially unchanged throughout the process. Another possible explanation of the differences seen in the maps is that some of the dark clouds may contain as yet undetected protostars, obscured by the high opacity apparent in the  $8.8\ \mu\text{m}$  MSX images. If a protostar is present, it can alter the local gas chemistry via grain mantle evaporation, which can change the emission morphologies (Jørgensen 2004). We are using data from the Spitzer Space Telescope to determine which dark clouds are truly starless and which contain embedded protostars in a sub-sample of these objects (Ragan et al. 2006, in prep.).

### 3.3. Distance Estimates

The kinematic distance to each dark cloud is calculated using the line center velocity and the Milky Way rotation curve model of Fich, Blitz, & Stark (1989). The distance assignments are presented in Table 3 for dark clouds for which we estimated masses. (Sources to which we are unable to assign a distance or those that show no significant emission are not subject to further calculations.) For every position, there is both a “near” and “far” distance solution that corresponds to the characteristic velocity of the emission. In addition to this ambiguity, Fich, Blitz, & Stark (1989) cite a  $\pm 14\%$  maximal deviation of the data from their rotation curve model; based on this consideration, we calculate errors in the distances and provide them in Table 3. In the cases where no error range (or an incomplete one) is given, no physical solution exists when calculating the distance with that error offset. For all subsequent calculations, we assume that the dark cloud is located at the “near” distance. We believe that this is a reasonable assumption since the clouds are seen in absorption against the Galactic mid-infrared background and, therefore, are unlikely to reside at the “far” distance. Assuming the “near” kinematical distance, which is also listed in Table 4, a typical core has a diameter of  $\sim 0.9$  pc.

Interestingly, the kinematical distances for the velocity component associated with the absorption are seldom coincident with the distances estimated for the UC HII region that was the original search target. In most cases we detect molecular emission at a single velocity, and no possible distance solution from the galactic rotation curve is consistent with the distance to the UC HII region. However, in the cases where there are multiple velocity components, the distance to the UC HII region is

often consistent with one of the kinematic distance solutions for a secondary velocity component. For example, G37.44+0.14 has a secondary detection of a component at  $18\ \text{km s}^{-1}$ , and the “far” distance associated with it ( $12.34$  kpc) is very close to the distance to the UC HII region ( $12.0$  kpc). In this case, it is likely that we are detecting two clouds along the same line of sight at different distances: one near the UC HII region and one nearer to us. Since the emission of the primary component corresponds so well to the absorbing dark cloud, we maintain that these lie at the “near” distances, though there is significant uncertainty in the distance calculation. Nonetheless, as we will show, these clouds are massive and are likely associated with the formation of intermediate and high-mass stars and stellar clusters.

### 3.4. Column Densities and Densities

To determine the molecular abundances relative to molecular hydrogen, we also need a measure of the total  $\text{H}_2$  column density. We estimate  $N(\text{H}_2)$  from the MSX images convolved to match the FCRAO beam resolution and the simple relation  $\tau_\lambda = \sigma_\lambda \cdot N(\text{H}_2)$ , where  $\tau_\lambda$  is the dust opacity,  $\sigma_\lambda$  is the dust extinction cross section, and  $N(\text{H}_2)$  is the column density of molecular hydrogen. The behavior of the mid-infrared extinction law is an area of active research. Recent results from Indebetouw et al. (2005), show agreement with Weingartner & Draine (2001) ( $R_v = 5.5$ , “case B”), we therefore adopt a value for  $\sigma_\lambda$  at  $8.8\ \mu\text{m}$  of  $2.3 \times 10^{-23}\ \text{cm}^2$ , though this value can be considered reliable only within a factor of 2. The opacity,  $\tau_\lambda$ , is roughly estimated by examining the relative intensities of the average background ( $I_{o,\lambda}$ ) and central core ( $I_\lambda$ ), assuming that  $I_\lambda = I_{o,\lambda}e^{-\tau_\lambda}$  (i.e. no emission by the core itself). The ratio  $I_\lambda/I_{o,\lambda}$  is related, but not identical, to the brightness contrast listed in Table 1, since the values listed in Table 1 do not incorporate the convolution to the FCRAO beam, and are provided at the original MSX resolution.

The column densities of  $\text{C}^{18}\text{O}$  and CS are estimated by assuming that the cores are in local thermodynamic equilibrium (LTE) at a temperature of  $15\ \text{K}$ , and that the emission is optically thin (Table 4). While the optically thin assumption is probably reasonable for  $\text{C}^{18}\text{O}$ , it probably does not hold for CS, which generally has optically thick emission in the interstellar medium. For  $\text{N}_2\text{H}^+$ , the fits to the hyperfine components generally suggest low optical depth, or  $\tau \sim 1$ . However, its emission is likely not in LTE. At a density of  $10^5\ \text{cm}^{-3}$ , the fractional population will be underestimated by a factor of  $\sim 1.7$  relative to LTE; we therefore apply this correction factor. We also crudely estimate the gas density by assuming the cloud is spherical and dividing the  $\text{H}_2$  column density by the diameter of the cloud (using the sizes listed in Table 1 and the distances in Table 3). This gives an average density of  $\approx 5000\ \text{cm}^{-3}$ . This is well below to the average densities found in other studies of regions of massive star formation using other tracers. For example, Plume et al. (1997) surveyed multiple transitions of CS in  $150\ \text{H}_2\text{O}$  masers (used as signposts of massive star formation) and found an average gas density of  $7.9 \times 10^5\ \text{cm}^{-3}$ . An obvious explanation for the lower density in our sample is that the clouds are not spherical, as we have naively assumed, and may instead be clumpy on scales below our resolution. Moreover, these objects are

likely at an earlier evolutionary state which is characterized by lower densities. A more detailed analysis of the density and column density will be presented in future work (Gibson et al. 2007, in prep.).

### 3.5. Masses

The total mass of each dark cloud is estimated using an assumed (“near”) distance, an approximate size based on the extent of molecular emission, the molecular column densities and approximate abundance calculated at the peak of absorption. Table 4 lists the masses of the objects for which there is a significant detection of  $\text{N}_2\text{H}^+$  or  $\text{C}^{18}\text{O}$  (or both) and a distance could be assigned. Since some of the dark clouds shown in Figure 1 have a different structure when viewed in different molecular tracers and may have different opacities, we have, for completeness, estimated the masses independently based on the abundances derived from both the  $\text{N}_2\text{H}^+$  and  $\text{C}^{18}\text{O}$  data. Our average mass is  $\approx 2000 - 3000 \text{ M}_\odot$  (depending on whether the  $\text{N}_2\text{H}^+$  or  $\text{C}^{18}\text{O}$  mass is used).

Figure 2 shows how the masses of our sample compare to the high-mass protostellar objects (HMPOs) presented in Williams et al. (2004), which were determined from submillimeter continuum emission. The masses for the HMPO sample are shown for both their “near” and “far” kinematic distances. Assuming that the sample encompasses objects at both the “near” and “far” kinematic distances, then the derived masses for HMPOs show a comparable range to our sources. One caveat with our comparison to the Williams et al. sample lies in the selection bias of our sample. As we will discuss below, our observations are only sensitive to relatively massive objects when the cores reside at such large distances. Furthermore, the HMPOs in the Williams et al. study also contain protostars which heat the surrounding environment and increase the dust emission. Therefore, in the warmer environments of the Williams et al. survey, lower mass cores would be easier to detect. The mass distribution shown in Figure 2 also shows good agreement with that found by Shirley et al. (2003), who observed CS emission from a sample of massive star forming regions and found a mean mass of  $920 \text{ M}_\odot$  with a large dispersion.

Several assumptions contribute to the uncertainty in the mass calculation, which is dominated by the error in the abundance calculation. We assume a constant temperature of 15 K, and a 5 K change in this value results in a  $\sim 20\%$  change in the abundance. The uncertainty in the dust opacity/column density relation contributes another factor of 2. Finally, we assume a constant abundance along the line of sight, which likely contributes an additional factor of 2 – 3 to the mass estimates.

We note that the typical distance to these clouds is  $\sim 4 \text{ kpc}$ , and with  $50''$  resolution, we are likely only sensitive to objects of some minimum mass. To examine this limit, we modeled the emission of a cloud assuming a constant density of  $10^5 \text{ cm}^{-3}$ , a radius of  $0.1 \text{ pc}$ , an  $\text{N}_2\text{H}^+$  abundance of  $5 \times 10^{-10}$  using a Monte Carlo radiation transfer model (Ashby et al. 2000). We estimate that our observations are capable of detecting clouds of mass greater than  $50\text{--}100 \text{ M}_\odot$  at a distance of  $4 \text{ kpc}$  with a  $50''$  beam.

Assuming that the “near” distance assumption is correct, the uncertainties mentioned above can account for

up to a factor of  $\sim 4 - 6$  in mass error, as the  $14\%$  error in translating the galactic rotation curve to kinematic distances only introduces a distance error of  $\sim 20\%$ . This accounting suggests that these objects are at least  $100 \text{ M}_\odot$ , and likely an order of magnitude more massive. Should the “near” distance assumption be incorrect and the dark clouds lie closer to the “far” kinematic distance, then the distance error dominates the calculation, and these clouds are substantially more massive.

### 3.6. Velocity Dispersion

The width of emission lines in star forming clouds serves as a useful diagnostic in determining the nature of a molecular region. According to Goldsmith (1987), the sites of massive star formation, GMCs, are characterized by large linewidths, while the isolated sites of low-mass star formation, dark clouds, have considerably smaller linewidths. We illustrate this range in Figure 3.

Caselli et al. (1998) derived linewidths for  $\text{N}_2\text{H}^+$  for a sample of low-mass, dense clumps in dark clouds, a site in which we expect to find narrow lines. The average linewidth in the Caselli et al. study was  $0.33 \text{ km s}^{-1}$  for clumps in which no IRAS source is detected. Current chemical models and observations indicate that  $\text{NH}_3$  and  $\text{N}_2\text{H}^+$  are related because  $\text{NH}_3$  likely forms via pathways linked  $\text{N}_2\text{H}^+$  (Aikawa et al. 2005). Therefore, we use the Harju et al. (1993) linewidths for  $\text{NH}_3$  clumps in Orion and Cepheus, known to be large regions of clustered, high-mass star formation for comparison. In addition, we include a comparison with linewidths of a sample of ammonia cores presented in Molinari et al. (1996), though we only include only the “Low” sources, a sample they argue have less luminous IRAS source, more quiescent envelopes, and, therefore, are younger than their “High” counterparts. In our sample, we find average linewidths of  $2.0 \text{ km s}^{-1}$  for  $\text{N}_2\text{H}^+$ ,  $2.1 \text{ km s}^{-1}$  for  $\text{C}^{18}\text{O}$ , and  $2.9 \text{ km s}^{-1}$  for CS. Though we see a broad range of line widths in the  $\text{N}_2\text{H}^+$  observations of the dark clouds, the characteristic line widths presented here are generally higher than those of the Harju et al. study and, to a greater extent, the Caselli et al. study, which implies that the objects in this sample are likely not associated with low-mass star formation. However, we find good agreement with the Molinari et al. sample.

For the CS  $J = 2 \rightarrow 1$  transition, the linewidths in the dark cloud sample are narrower than those observed by Plume et al. (1997) in survey of massive star forming regions, which averaged  $4.2 \text{ km s}^{-1}$  in this line. However, since Plume et al. surveyed regions known to have undergone massive star formation, it is possible that the current generation of massive stars are injecting additional turbulence into the surrounding environment. Similarly, the Shirley et al. (2003) study observed the CS  $J = 5 \rightarrow 4$  transition in star-forming cores and found linewidths averaging  $5.6 \text{ km s}^{-1}$ . The narrower lines in the dark clouds indicates that they are still relatively quiescent and suggest that may, indeed, be pre-cursor sites of intermediate or massive star formation.

## 4. SUMMARY

We have identified 41 infrared dark (at  $8.8 \mu\text{m}$ ) clouds that are opaque, compact, and associated with UC HII regions using MSX survey data. In order to determine some basic characteristics of these dark clouds, we have

mapped emission from  $N_2H^+ 1 \rightarrow 0$ ,  $CS 2 \rightarrow 1$  and  $C^{18}O 1 \rightarrow 0$  using the FCRAO. The morphology and relative strengths of these molecular lines varies dramatically, possibly indicating evolutionary differences and/or the presence of undetected embedded protostar(s). Based on the derived kinematic distances and the simplifying assumption that the cores are optically thin, we have determined average properties: diameter  $< D > \approx 0.9$  pc, density  $< n > \approx 5000 \text{ cm}^{-3}$ , and mass  $< M > \approx 2500 M_\odot$ . The low density estimate likely indicates that the dark clouds are clumpy rather than homogeneous. The derived masses, however, are comparable to those derived for a sample of HMPOs. The linewidths are larger than those seen in low-mass star forming cores and larger than in high-mass star forming cores in Orion and Cepheus. However, they are narrower than the CS linewidths seen

in regions that are actively forming massive stars. These observations, taken together, suggest that the infrared dark clouds may be the relatively quiescent pre-cursors to intermediate or massive star formation, the so-called “pre-protostellar cores.” At present, we do not know if these sources are truly starless. Only by obtaining very sensitive infrared observations can we confirm the starless nature of these cores.

We are grateful to the referee for a very thorough report, which improved this paper. We are grateful to J. Weingartner for providing detailed dust opacity coefficients. This research has made use of the SIMBAD database, operated at CDS, Strasbourg, France

## APPENDIX

### COINCIDENT SOURCES

The coordinates of each dark region were examined by the *Set of Identifications, Measurements, and Bibliography for Astronomical Data (SIMBAD)* database in search of associated objects indicative of active star formation (e.g. masers, IRAS sources, radio sources). In most cases, the searches yielded no results, but some revealed objects within one arcminute of the dark region’s coordinates. Below, we summarize any associations with the objects for which we present emission maps. We note that whenever coincident sources are found, we provide the offsets relative to the central absorption peak position given in Table 1.

*G09.21–0.22* There is an IRAS source (IRAS 18038-2105;  $\alpha(2000) = 18^h06^m53.1^s$ ,  $\delta(2000) = -21^\circ04'38''$ ) in the vicinity of this absorbing cloud, offset by 0'78 from the center of the dark region.

*G09.88–0.11* This region has an associated 1612 MHz OH maser which is cited in Blommaert, Van Langevelde, and Michaels (1994). This source, OH 9.878-0.127, has a position of  $\alpha(2000) = 18^h07^m59^s.07$ ,  $\delta(2000) = -20^\circ27'34''.3$ , which is offset from the center of our region by 1'05. This object may be associated with a circumstellar shell around an evolved star, and the velocities believed to correspond to the expanding shells of material are 79.5 and 111.3  $\text{km s}^{-1}$ , which is not coincident with the velocity of the emission detected here (17  $\text{km s}^{-1}$ ).

*G10.59–0.31* This region contains a radio source, located at  $\alpha(2000) = 18^h10^m6^s.18$ ,  $\delta(2000) = -19^\circ55'33''.11$ , according to Zoonematkermani et al. (1990), which is offset from the center of our region by 0'44.

*G12.50–0.22* There is an IRAS source (IRAS 18197-1812;  $\alpha(2000) = 18^h13^m39^s.0$ ,  $\delta(2000) = -18^\circ11'46''$ ) offset by 0'96 from the absorbing region.

*G19.37–0.03* This region is near a known UC HII region, with a water and methanol maser (Codella & Felli 1995; Szymczak et al. 2000) also identified in the vicinity ( $\alpha(2000) = 18^h26^m24^s.3$ ,  $\delta(2000) = -12^\circ3'46''$ , offset 0'85 from the absorbing region. The peak velocity of this maser is 26.3  $\text{km s}^{-1}$  (Szymczak et al. 2000), which is consistent with the velocity of our measured emission (27  $\text{km s}^{-1}$ ). Molinari et al. (1996) also observed this maser site and designated it as Mol 55.

*G30.89+0.14* This region has an associated methanol maser, as described by Szymczak et al. (2000). The maser is located at  $\alpha(2000) = 18^h47^m14^s.99$ ,  $\delta(2000) = -1^\circ44'7''.99$ , which is offset from the center of our region by 0'99. Szymczak et al. (2000), using a 6.7 GHz survey, measured the internal velocity of the maser source to be  $\approx 105 \text{ km/s}$ , the velocity of the peak to be 101.5  $\text{km/s}$ . This is consistent with one of the velocity components we measured in this object (108  $\text{km s}^{-1}$ ).

*G32.01+0.05* This region has an associated IRAS point source (18470-0050) which is offset from the center of our region by 1'00 at  $\alpha(2000) = 18^h49^m36^s.6$ ,  $\delta(2000) = -00^\circ46'51''$  which coincides with a radio source (Becker et al. 1994). This was confirmed to be a methanol maser (observed in the velocity range between 91 and 102  $\text{km s}^{-1}$ ) by van der Walt et al. (1995), which is consistent with the emission we observed at 95  $\text{km s}^{-1}$ .

*G34.74–0.12* This region has an associated IRAS point source (18526+0130) which is offset from the center of our region by 0'80 at  $\alpha(2000) = 18^h55^m10^s$ ,  $\delta(2000) = +1^\circ33'57''$ .

## REFERENCES

- |   |   |
|---|---|
| <p>Aikawa, Y., Herbst, E., Roberts, H., &amp; Caselli, P. 2005, ApJ, 620, 330</p> <p>Alves, J. F., Lada, C. J., &amp; Lada, E. A. 2001, Nature, 409, 159</p> <p>André, P., Ward-Thompson, D., &amp; Barsony, M. 2000, Protostars and Planets IV, 59</p> <p>Ashby, M. L. N., et al. 2000, ApJ, 539, L115</p> <p>Bacmann, A., André, P., Puget, J.-L., Abergel, A., Bontemps, S., &amp; Ward-Thompson, D. 2000, A&amp;A, 361, 555</p> | <p>Becker, R. H., White, R. L., Helfand, D. J., &amp; Zoonematkermani, S. 1994, ApJS, 91, 347</p> <p>Beichman, C. A., Myers, P. C., Emerson, J. P., Harris, S., Mathieu, R., Benson, P. J., &amp; Jennings, R. E. 1986, ApJ, 307, 337</p> <p>Bergin, E. A. &amp; Langer, W. D. 1997, ApJ, 486, 316</p> <p>Blommaert, J. A. D. L., van Langevelde, H. J., &amp; Michiels, W. F. P. 1994, A&amp;A, 287, 479</p> |
|---|---|

- Buisson, G., Desbats, L., Duvert, G., Forveille, T., Gras, R., Guilloteau, S., Lucas, R., & Valiron, P. 2002, *Continuum and Line Analysis Single-dish System Manual*, (CLASS; IRAM: Grenoble; <http://iram.fr/GS/class/class.html>)
- Carey, S. J., Clark, F. O., Egan, M. P., Price, S. D., Shipman, R. F., & Kuchar, T. A. 1998, *ApJ*, 508, 721
- Caselli, P., Benson, P., Myers, P., & Tafalla, M. 2002, *ApJ*, 572, 238
- Codella, C., & Felli, M. 1995, *A&A*, 302, 521
- H. M. 1984, *ApJ*, 285, 89
- Egan, M. P., Shipman, R. F., Price, S. D., Carey, S. J., Clark, F. O., & Cohen, M. 1998, *ApJ*, 494, L199
- Fich, M., Blitz, L., & Stark, A. 1989, *ApJ*, 342, 272
- Garay, G. & Lizano, S. 1999, *PASP*, 111, 1049
- Gibson, D. L., Plume, R., Bergin, E. A., & Ragan, S. E., 2007, in preparation
- Goldsmith, P. 1987, *Interstellar processes; Proceedings of the Symposium*, Dordrecht, D. Reidel Publishing Co., p. 51-70.
- Harju, J., Walmsley, C. M., & Wouterloot, J. G. A. 1993, *A&AS*, 98, 51
- Indebetouw, R., et al. 2005, *ApJ*, 619, 931
- Jørgensen, J. K. 2004, *A&A*, 424, 589
- Lee, J.-E., Bergin, E. A., & Evans, N. J. 2004, *ApJ*, 617, 360
- Lee, C. W. & Myers, P. C. 1999, *ApJS*, 123, 233
- Menten, K. M., Pillai, T., & Wyrowski, F. 2005, *IAUS*, 227, 23
- Molinari, S., Brand, J., Cesaroni, R., & Palla, F. 1996, *A&A*, 308, 573
- Myers, P. C. & Benson, P. J. 1983, *ApJ*, 266, 309
- Pillai, T., Wyrowski, F., Carey, S. J., & Menten, K. M. 2006, *A&A*, 450, 569
- Plume, R., Jaffe, D. T., Evans, N. J. II, Martín-Pintado, J., & Gómez-González, J. 1997, *ApJ*, 476, 730
- Ragan, S. E., Bergin, E. A., Plume, R., & Gibson, D. L. 2006, in preparation
- Rathborne, J. M., Jackson, J. M., & Simon, R. 2006, *ApJ*, 641, 389
- Shirley, Y. L., Evans, N. J. II, Young, K. E., Knez, C., & Jaffe, D. T. 2003, *ApJS*, 149, 375
- Sridharan, T. K., Beuther, H., Saito, M., Wyrowski, F., & Schilke, P. 2005, *ApJ*, 634, 57
- Szymczak, M., Hrynek, G., & Kus, A. J. 2000, *A&AS*, 143, 269
- Tafalla, M., Myers, P. C., Caselli, P., Walmsley, C. M., & Comito, C. 2002, *ApJ*, 569, 815
- van der Walt, D. J., Gaylard, M. J., & MacLeod, G. C. 1995, *A&AS*, 110, 81
- Weingartner, J. C., & Draine, B. T. 2001, *ApJ*, 548, 296
- Williams, S. J., Fuller, G. A., & Sridharan, T. K. 2004, *A&A*, 417, 115
- Wood, D. O. S. & Churchwell, E. 1989, *ApJS*, 69, 831
- Zinnecker, H., McCaughrean, M. J., & Wilking, B. A. 1993, *Protostars and Planets III*, 429
- Zoonematkermani, S., Helfand, D. J., Becker, R. H., White, R. L., & Perley, R. A. 1990, *ApJS*, 74, 181

TABLE 1  
BASIC PROPERTIES OF THE TARGET MSX PRE-STELLAR CORES

H II Region	Name	Galactic Coordinates		Position		Major Axis ( $'$ )	Minor Axis ( $'$ )	Brightness Contrast	Bandwidth <sup>a</sup> ( $\text{km s}^{-1}$ )
		$l$ ( $^{\circ}$ )	$b$ ( $^{\circ}$ )	$\alpha(2000)$ ( $h : m : s$ )	$\delta(2000)$ ( $^{\circ} : ' : ''$ )				
G0589	G5.85−0.23	5.854	−0.231	17:59:49.50	−24:00:50.25	0.64	0.60	0.409	−20 − 112
	G6.01−0.38	6.013	−0.384	18:00:45.13	−23:57:07.10	1.90	0.78	0.427	...
	G6.26−0.51	6.263	−0.511	18:01:46.57	−23:47:51.61	1.38	0.93	0.587	−25 − 107
G0867	G8.56+0.42	8.559	0.415	18:03:11.72	−21:20:37.48	0.40	0.36	0.286	...
	G8.64−0.09	8.636	−0.086	18:05:13.98	−21:31:21.58	0.60	0.35	0.292	...
	G9.16+0.06	9.156	0.060	18:05:46.71	−20:59:51.77	0.80	0.46	0.340	−25 − 107
	G9.20−0.20	9.204	−0.199	18:06:50.86	−21:04:56.00	0.80	0.47	0.288	...
	G9.21−0.22	9.213	−0.217	18:06:56.03	−21:04:59.32	0.80	0.60	0.313	−35 − 113
	G9.28−0.15	9.281	−0.152	18:06:49.96	−20:59:31.46	1.60	0.64	0.431	−38 − 116
	G9.64+0.18	9.626	0.184	18:06:17.86	−20:31:37.28	0.23	0.15	0.120	...
	G9.80−0.15	9.796	−0.151	18:07:54.07	−20:32:30.17	0.90	0.68	0.242	...
	G9.85−0.14	9.846	−0.139	18:07:57.60	−20:29:31.81	1.20	0.80	0.254	...
	G9.86−0.04	9.856	−0.039	18:07:36.47	−20:26:05.34	1.24	0.61	0.371	−35 − 113
	G9.88−0.11	9.881	−0.111	18:07:55.69	−20:26:52.74	1.10	0.91	0.403	−35 − 113
	G10.27+0.19	10.274	0.186	18:07:38.17	−19:57:36.60	0.56	0.53	0.183	...
	G10.59−0.31	10.588	−0.311	18:10:08.02	−19:55:34.98	1.00	0.48	0.295	−35 − 113
	G10.70−0.33	10.704	−0.325	18:10:25.44	−19:49:53.70	1.00	0.84	0.367	−60 − 86
	G10.74−0.13	10.743	−0.127	18:09:46.03	−19:42:06.37	5.20	1.50	0.600	...
	G10.74+0.01	10.743	0.005	18:09:16.59	−19:38:16.41	1.23	0.93	0.413	...
	G10.99−0.09	10.989	−0.086	18:10:07.18	−19:27:59.72	0.80	0.58	0.593	−60 − 86
	G11.13+0.11	11.126	0.114	18:09:39.49	−19:14:59.92	0.58	0.45	0.239	...
	G11.13−0.13	11.131	−0.129	18:10:34.21	−19:21:46.84	2.40	0.60	0.463	...
	G11.23+0.07	11.226	0.068	18:10:02.01	−19:11:04.88	1.22	0.27	0.202	...
	G11.24+0.07	11.241	0.066	18:10:04.30	−19:10:21.11	1.03	0.52	0.283	...
	G12.22+0.14	12.219	0.138	18:11:47.79	−18:16:51.43	1.68	0.80	0.388	−35 − 113
	G12.50−0.22	12.498	−0.222	18:13:41.44	−18:12:32.16	0.88	0.75	0.475	−35 − 113
	G12.58+0.27	12.578	0.273	18:12:01.49	−17:54:04.62	1.55	0.61	0.263	...
	G12.61+0.25	12.608	0.248	18:12:10.65	−17:53:13.15	0.86	0.59	0.235	...
	G12.74−0.36	12.736	−0.361	18:14:41.01	−18:03:59.01	0.87	0.52	0.280	...
	G14.33−0.57	14.334	−0.567	18:18:37.67	−16:45:30.54	0.97	0.51	0.362	−54 − 93
	G14.38−0.46	14.384	−0.457	18:18:19.32	−16:39:44.47	1.36	0.76	0.268	...
	G14.40−0.60	14.398	−0.604	18:18:53.43	−16:43:10.49	1.51	1.51	0.412	...
	G14.49−0.15	14.493	−0.146	18:17:23.71	−16:25:08.20	1.68	0.90	0.465	...
	G14.64−0.57	14.636	−0.571	18:19:14.32	−16:29:39.47	2.25	0.90	0.568	...
	G14.65−0.18	14.648	−0.117	18:17:35.72	−16:16:07.42	0.70	0.32	0.346	...
	G15.05+0.09	15.053	0.089	18:17:38.41	−15:48:52.11	1.60	0.63	0.532	...
	G15.55−0.45	15.548	−0.447	18:20:34.52	−15:37:54.30	0.88	0.48	0.280	...
	G19.25−0.07	19.246	−0.069	18:26:20.57	−12:11:16.74	0.70	0.39	0.238	...
	G19.28−0.39	19.281	−0.387	18:27:33.68	−12:18:18.35	1.08	0.78	0.417	−35 − 113
	G19.29+0.08	19.291	0.078	18:25:53.80	−12:04:46.57	2.75	1.10	0.447	...
	G19.35−0.04	19.348	−0.039	18:26:25.72	−12:05:01.46	0.72	0.68	0.275	...
	G19.37−0.03	19.374	−0.034	18:26:27.61	−12:03:30.32	1.01	0.80	0.375	−35 − 113
	G19.40−0.01	19.396	−0.006	18:26:24.05	−12:01:33.28	1.05	0.94	0.330	−35 − 113
	G19.91−0.21	19.913	−0.207	18:28:06.69	−11:39:42.83	1.39	0.98	0.346	...
	G19.97−0.11	19.967	−0.106	18:27:50.94	−11:34:01.67	0.65	0.65	0.275	...
	G19.98−0.21	19.979	−0.212	18:28:15.29	−11:36:20.91	1.57	0.72	0.318	...
	G23.32+0.06	23.318	0.056	18:33:34.18	−08:31:19.32	2.10	0.42	0.259	...
	G23.37−0.29	23.368	−0.287	18:34:53.66	−08:38:08.59	0.72	0.50	0.376	37 − 183
	G23.38−0.13	23.378	−0.126	18:34:20.09	−08:33:09.71	0.77	0.40	0.321	...
	G23.38−0.51	23.381	−0.521	18:35:45.56	−08:43:54.76	0.71	0.60	0.227	...
	G23.38+0.29	23.383	0.288	18:32:51.52	−08:21:26.29	0.57	0.50	0.311	...
	G23.44−0.52	23.441	−0.524	18:35:52.89	−08:40:47.92	1.88	0.53	0.313	...
	G23.48+0.11	23.476	0.106	18:33:41.10	−08:21:31.62	1.22	0.54	0.378	...
	G23.48−0.53	23.481	−0.534	18:35:59.52	−08:38:56.65	1.50	0.50	0.480	−35 − 113
	G23.61−0.01	23.614	−0.009	18:34:21.28	−08:17:21.61	1.82	0.76	0.471	...
	G24.05−0.22	24.051	−0.216	18:35:54.61	−07:59:48.07	0.81	0.51	0.368	37 − 184
	G24.16+0.08	24.158	0.078	18:35:03.29	−07:45:58.96	0.90	0.84	0.390	37 − 184
	G24.17+0.06	24.170	0.064	18:35:07.65	−07:45:43.85	0.71	0.37	0.344	...
	G24.37−0.16	24.369	−0.157	18:36:17.34	−07:41:13.82	1.68	1.56	0.467	...
	G24.37−0.21	24.371	−0.214	18:36:29.82	−07:42:41.72	2.10	0.96	0.258	...
	G24.44−0.23	24.436	−0.234	18:36:41.36	−07:39:46.99	1.54	1.51	0.546	...
	G24.63+0.15	24.629	0.148	18:35:40.73	−07:18:57.64	2.15	0.70	0.533	...
	G25.08+0.20	25.076	0.199	18:36:19.50	−06:53:44.33	0.80	0.63	0.363	...
	G25.24−0.22	25.243	−0.216	18:38:07.16	−06:56:16.48	0.72	0.56	0.298	...
	G25.25−0.24	25.248	−0.236	18:38:12.01	−06:56:33.53	1.00	0.50	0.283	...
	G25.61+0.24	25.613	0.239	18:37:10.53	−06:24:01.14	1.70	1.70	0.374	...
	G25.99−0.06	25.985	−0.057	18:38:55.26	−06:12:20.39	1.03	0.80	0.337	−35 − 113
	G30.14−0.07	30.135	−0.069	18:46:34.71	−02:31:13.90	1.40	0.60	0.287	−35 − 113
	G30.31−0.28	30.309	−0.282	18:47:39.31	−02:27:46.38	0.82	0.63	0.226	...
	G30.49−0.39	30.494	−0.392	18:48:23.10	−02:20:54.35	0.84	0.81	0.414	22 − 168
	G30.53−0.27	30.353	−0.272	18:47:42.00	−02:25:08.99	1.25	0.91	0.310	−35 − 113
	G30.58−0.25	30.579	−0.252	18:48:02.48	−02:12:32.12	1.53	0.58	0.305	...

TABLE 1 — *Continued*

H II Region	Name	Galactic Coordinates		Position		Major Axis (')	Minor Axis (')	Brightness Contrast	Bandwidth <sup>a</sup> (km s <sup>-1</sup> )
		<i>l</i>	<i>b</i>	$\alpha(2000)$	$\delta(2000)$				
		(°)	(°)	(h : m : s)	(° : ' : ")				
G3141	G30.66+0.05	30.663	0.046	18:47:08.00	-01:59:53.60	1.82	0.80	0.358	...
	G30.69+0.06	30.689	0.056	18:47:08.72	-01:58:13.85	0.75	0.63	0.217	...
	G30.89+0.14	30.894	0.136	18:47:14.08	-01:45:05.75	1.60	0.60	0.321	-35 – 113
	G30.98-0.15	30.978	-0.148	18:48:23.97	-01:48:23.07	1.33	0.80	0.411	-35 – 113
	G31.02-0.12	31.024	-0.116	18:48:22.17	-01:45:03.19	1.62	0.70	0.450	-35 – 113
	G31.23+0.02	31.226	0.024	18:50:03.85	-00:37:02.40	1.20	0.80	0.361	...
	G31.39+0.30	31.391	0.296	18:47:34.34	-01:14:10.89	2.10	1.70	0.349	...
G3350	G31.70-0.50	31.699	-0.496	18:50:57.27	-01:19:24.42	0.68	0.50	0.348	...
	G31.71-0.49	31.723	-0.486	18:50:57.76	-01:17:51.09	0.63	0.60	0.336	...
	G32.01+0.05	32.013	0.056	18:49:33.70	-00:47:32.25	1.17	1.10	0.526	-35 – 113
	G32.84-0.03	32.843	-0.032	18:51:23.35	-00:05:37.42	1.30	0.97	0.357	...
	G33.36-0.01	33.363	-0.007	18:52:14.91	00:22:49.67	1.58	0.84	0.288	...
	G33.42+0.13	33.418	0.126	18:51:52.52	00:29:24.18	0.44	0.25	0.217	...
	G33.70-0.02	33.699	-0.016	18:52:53.60	00:40:31.43	1.80	0.50	0.250	...
G3426	G33.82-0.22	33.819	-0.219	18:53:50.10	00:41:22.54	0.90	0.53	0.432	2 – 149
	G34.13+0.08	34.134	0.076	18:53:21.57	01:06:16.14	1.68	0.50	0.254	...
	G34.26+0.19	34.263	0.189	18:53:11.55	01:16:14.93	1.75	0.61	0.271	...
	G34.74-0.12	34.739	-0.122	18:55:10.11	01:33:09.25	0.90	0.80	0.393	-15 – 131
	G34.74+0.01	34.744	0.006	18:54:43.32	01:36:55.46	0.75	0.57	0.212	...
	G35.04-0.47	35.043	-0.474	18:56:58.62	01:39:44.74	0.65	0.41	0.312	...
	G34.63-1.03	34.627	-1.026	18:58:10.95	01:02:25.33	0.26	0.18	0.447	-29 – 117
G3520	G34.78-0.80	34.778	-0.804	18:57:40.08	01:16:33.76	0.56	0.45	0.341	-35 – 114
	G35.02-1.50	35.018	-1.497	19:00:34.38	01:10:23.16	0.97	0.35	0.375	...
	G35.20-0.72	35.203	-0.721	18:58:08.92	01:41:31.31	0.78	0.51	0.436	-29 – 117
	G37.08-0.15	37.081	-0.149	18:59:32.80	03:37:25.91	0.42	0.40	0.321	...
	G37.25+0.01	37.253	0.011	18:59:17.48	03:50:59.94	0.98	0.52	0.296	...
	G37.42+0.17	37.418	0.173	18:59:00.95	04:04:14.78	0.70	0.64	0.342	...
	G37.44+0.14	37.439	0.138	18:59:10.75	04:04:24.37	0.79	0.40	0.322	-35 – 113
G4318	G37.89-0.15	37.886	-0.152	19:01:02.00	04:20:18.23	1.03	0.58	0.325	-26 – 107
	G43.19-0.16	43.187	-0.162	19:10:53.01	09:02:30.58	0.42	0.20	0.304	...
	G43.32-0.20	43.318	-0.204	19:11:16.78	09:08:18.83	0.50	0.42	0.165	...
	G43.78+0.05	43.776	0.046	19:11:14.38	09:39:36.89	0.92	0.91	0.377	-23 – 124
	G43.64-0.82	43.644	-0.824	19:14:07.05	09:08:24.64	0.60	0.21	0.577	-19 – 127
	G44.29-0.09	44.291	-0.092	19:12:42.25	10:03:10.40	0.71	0.46	0.219	...
	G5023	48.836	0.151	19:20:29.90	14:11:12.12	1.22	0.58	0.317	...
G5031	G48.84+0.14	48.848	0.136	19:20:34.57	14:11:24.84	0.70	0.43	0.242	...
	G50.07+0.06	50.071	0.059	19:23:14.36	15:13:58.11	0.86	0.33	0.378	-13 – 133
	G51.00-0.18	51.001	-0.177	19:22:55.92	15:56:24.24	0.60	0.35	0.290	...
	G53.88-0.18	53.879	-0.181	19:31:42.73	18:27:55.78	1.12	0.42	0.417	-30 – 116
	G6148	61.519	0.024	19:47:09.72	25:13:00.46	0.60	0.45	0.334	...
	G7578	75.753	0.749	20:19:57.75	37:39:01.90	1.10	0.90	0.474	-33 – 113
	G76.38+0.63	76.381	0.626	20:22:17.04	38:05:50.23	0.40	0.30	0.318	-33 – 113

<sup>a</sup> For observed regions, we give the total velocity range to which the observations were sensitive. A given object was probed in the same velocity range for each observed transition.

TABLE 2  
MOLECULAR LINE OBSERVATIONS

Source	$\Delta\alpha$ (')	$\Delta\delta$ (')	$\text{N}_2\text{H}^+ \text{ J=1-0}$			$\text{C}^{18}\text{O J=1-0}$			$\text{CS J=2-1}$		
			$\int T_A^* dv$ (K km s <sup>-1</sup> )	V (km s <sup>-1</sup> )	$\Delta v$ (km s <sup>-1</sup> )	$\int T_A^* dv$ (K km s <sup>-1</sup> )	V (km s <sup>-1</sup> )	$\Delta v$ (km s <sup>-1</sup> )	$\int T_A^* dv$ (K km s <sup>-1</sup> )	V (km s <sup>-1</sup> )	$\Delta v$ (km s <sup>-1</sup> )
G05.85−0.23	0.4	−0.4	1.21(0.15)	17.2(0.1)	0.8(0.1)	1.44(0.17)	17.0(0.1)	1.7(0.2)	0.47(0.10)	16.9(0.2)	2.2(0.3)
G06.26−0.51	0.0	0.0	(<0.15)	...	...	1.69(0.11)	22.7(0.1)	2.3(0.2)	1.64(0.15)	23.2(0.2)	4.2(0.5)
G09.16+0.06	0.0	0.0	(<0.12)	...	...	1.39(0.09)	31.3(0.1)	1.7(0.1)	0.40(0.07)	31.3(0.1)	1.2(0.3)
G09.21−0.22	0.0	0.0	3.59(0.15)	42.8(0.1)	1.8(0.2)	...	...	...	1.29(0.11)	42.7(0.1)	2.8(0.3)
G09.28−0.15	0.0	0.0	3.66(0.10)	41.4(0.1)	1.9(0.4)	...	...	...	1.27(0.12)	41.3(0.1)	2.6(0.3)
G09.86−0.04	0.0	0.0	0.87(0.11)	18.1(0.1)	1.1(0.2)	...	...	...	1.52(0.14)	17.8(0.1)	2.3(0.2)
G09.88−0.11	0.0	0.0	(<0.13)	...	...	...	...	...	0.54(0.15)	17.3(0.2)	1.8(0.6)
G10.59−0.31	0.0	0.0	(<0.40)	...	...	...	...	...	(<0.24)	...	...
G10.70−0.33	0.0	0.0	(<0.13)	...	...	...	...	...	(<0.13)	...	...
G10.99−0.09	0.0	0.0	4.24(0.11)	29.6(0.1)	2.4(0.2)	2.25(0.17)	29.5(0.1)	2.2(0.2)	1.00(0.12)	29.2(0.3)	4.2(0.5)
G12.22+0.14	0.0	0.0	3.60(0.08)	39.6(0.1)	1.7(0.1)	...	...	...	1.78(0.07)	36.7(0.1)	2.2(0.1)
G12.50−0.22	0.0	0.0	2.97(0.10)	35.8(0.1)	1.8(0.1)	1.60(0.13)	35.7(0.1)	1.8(0.2)	1.40(0.10)	35.6(0.1)	2.0(0.2)
G14.33−0.57a	0.0	0.0	(<0.14)	...	...	2.19(0.15)	19.3(0.1)	2.1(0.2)	1.25(0.13)	19.6(0.1)	2.4(0.3)
G14.33−0.57b	−1.7	0.8	1.42(0.14)	20.0(0.1)	1.1(0.2)	1.81(0.12)	19.9(0.1)	1.6(0.2)	0.84(0.10)	20.3(0.1)	1.4(0.2)
G19.28−0.39	0.0	0.0	(<0.17)	...	...	...	...	...	0.26(0.07)	54.0(0.1)	1.1(0.2)
G19.37−0.03	0.0	0.0	3.62(0.11)	27.3(0.1)	2.5(0.1)	...	...	...	3.02(0.07)	27.0(0.1)	3.8(0.1)
G19.40−0.01	0.0	0.0	0.95(0.11)	27.0(0.1)	1.2(0.3)	...	...	...	0.81(0.06)	26.5(0.1)	2.9(0.3)
G23.37−0.29	0.0	0.0	2.88(0.27)	78.5(0.1)	2.0(0.2)	3.97(0.21)	78.1(0.1)	2.7(0.2)	2.30(0.12)	77.8(0.1)	4.8(0.3)
G23.48−0.53a	0.0	0.0	1.45(0.12)	64.8(0.1)	2.5(0.4)	...	...	...	0.90(0.09)	63.9(0.3)	4.8(0.6)
G23.48−0.53b	−2.1	−2.1	1.24(0.12)	62.8(0.1)	2.9(0.4)	...	...	...	0.73(0.08)	62.7(0.3)	2.9(0.4)
G24.05−0.22	0.0	0.0	2.71(0.21)	81.4(0.1)	1.9(0.3)	2.30(0.10)	81.5(0.1)	2.0(0.1)	1.00(0.13)	82.0(0.2)	2.8(0.5)
G24.16+0.08	0.0	0.0	(<0.10)	...	...	1.64(0.16)	51.8(0.1)	1.9(0.2)	(<0.10)	...	...
G25.99−0.06	0.0	0.0	0.80(0.15)	89.9(0.3)	1.6(0.5)	...	...	...	1.05(0.11)	90.2(0.1)	2.4(0.3)
G30.14−0.07	0.0	0.0	(<0.12)	...	...	...	...	...	(<0.15)	86.8(0.2) <sup>a</sup>	2.7(0.5) <sup>a</sup>
G30.49−0.39	1.2	−0.8	(<0.14)	...	...	...	...	...	0.62(0.12)	106.4(0.3)	3.0(0.9)
G30.53−0.27	0.0	0.0	(<0.12)	...	...	...	...	...	1.73(0.19)	102.9(0.4)	7.3(0.9)
G30.89+0.14	0.0	0.0	1.29(0.13)	96.5(0.2)	3.4(0.3)	...	...	...	0.56(0.10)	95.9(0.3)	3.0(0.5)
G30.98−0.15	−0.4	0.0	4.56(0.12)	77.9(0.1)	2.6(0.1)	...	...	...	2.27(0.11)	77.9(0.1)	4.3(0.2)
G31.02−0.12	0.0	0.0	1.57(0.07)	76.6(0.1)	2.2(0.2)	1.24(0.11)	76.2(0.1)	3.0(0.3)	0.66(0.08)	76.6(0.2)	3.3(0.4)
G32.01+0.05	0.0	0.0	7.18(0.10)	95.3(0.1)	3.9(0.1)	4.42(0.12)	97.2(0.1)	4.7(0.2)	4.03(0.09)	96.0(0.1)	6.8(0.2)
G33.82−0.22	0.0	0.0	1.03(0.11)	11.3(0.1)	1.0(0.3)	...	...	...	0.48(0.09)	11.5(0.1)	1.0(0.2)
G34.63−1.03	0.0	0.0	1.16(0.15)	13.6(0.2)	2.6(0.6)	0.58(0.08)	12.8(0.1)	1.1(0.2)	(<0.15)	...	...
G34.74−0.12	0.0	0.0	1.92(0.17)	79.1(0.1)	2.7(0.3)	3.51(0.14)	78.9(0.2)	2.1(0.1)	1.11(0.10)	78.9(0.2)	3.8(0.4)
G34.78−0.80	0.0	0.0	0.33(0.11)	43.2(0.4)	3.0(0.7)	2.25(0.10)	44.1(0.1)	3.3(0.1)	1.83(0.07)	43.5(0.1)	3.0(0.2)
G35.20−0.72	0.0	0.0	3.02(0.20)	33.1(0.1)	2.5(0.3)	2.04(0.12)	33.2(0.1)	1.9(0.1)	1.91(0.13)	33.2(0.1)	3.4(0.3)
G37.44+0.14a	0.0	0.0	(<0.10)	...	...	1.14(0.06)	40.0(0.1)	1.6(0.1)	0.77(0.04)	40.1(0.1)	1.4(0.1)
G37.44+0.14b	−2.5	−0.4	0.65(0.08)	17.8(0.1)	0.5(0.1)	0.52(0.04)	17.8(0.1)	0.7(0.1)	0.25(0.03)	17.7(0.1)	0.9(0.1)
G37.89−0.15	0.0	0.0	0.45(0.08)	12.9(0.1)	0.7(0.1)	0.63(0.04)	12.9(0.1)	0.7(0.1)	0.36(0.04)	13.0(0.1)	0.7(0.1)
G43.64−0.82	0.4	2.4	(<0.25)	...	...	...	...	...	0.25(0.05)	85.4(0.1)	0.5(0.1)
G43.78+0.05	0.0	0.0	(<0.17)	...	...	...	...	...	(<0.09)	...	...
G50.07+0.06	−0.8	−0.8	(<0.19)	...	...	...	...	...	0.73(0.08)	54.8(0.1)	1.5(0.2)
G53.88−0.18	0.0	0.0	(<0.21)	...	...	...	...	...	(<0.12)	...	...
G75.75+0.75	0.0	0.0	(<0.12)	...	...	...	...	...	(<0.07)	...	...
G76.38+0.63	0.0	0.0	(<0.15)	...	...	...	...	...	(<0.07)	...	...

<sup>a</sup> Non-detection of CS in single scan. Average of 25 scans detects a weak line at the 5 $\sigma$  level. The velocity and line width from this average are provided in the table.

TABLE 3  
KINEMATIC DISTANCES TO SEPARATED VELOCITY COMPONENTS

Source	Velocity Component (km s <sup>-1</sup> )	Near Distance (kpc)	Far Distance (kpc)	Adopted Distance (kpc)	UCHII region Distance (kpc)
G05.85−0.23	17	3.14 <sup>+0.66</sup> <sub>−0.76</sub>	13.78 <sup>+0.75</sup> <sub>−0.67</sub>	3.14	2.6
	9	1.53 <sup>+0.86</sup> <sub>−0.96</sub>	15.38 <sup>+0.97</sup> <sub>−0.86</sub>		
G06.26−0.51	23	3.78 <sup>+0.59</sup> <sub>−0.67</sub>	13.12 <sup>+0.67</sup> <sub>−0.60</sub>	3.78	2.6
	17	3.01 <sup>+0.68</sup> <sub>−0.77</sub>	13.89 <sup>+0.77</sup> <sub>−0.68</sub>		
G09.16+0.06	31	3.81 <sup>+0.61</sup> <sub>−0.69</sub>	12.97 <sup>+0.61</sup> <sub>−0.59</sub>	3.81	6.2
G09.21−0.22	43	4.57 <sup>+0.53</sup> <sub>−0.59</sub>	12.21 <sup>+0.59</sup> <sub>−0.53</sub>	4.57	6.2
G09.28−0.15	42	4.48 <sup>+0.54</sup> <sub>−0.61</sub>	12.30 <sup>+0.61</sup> <sub>−0.54</sub>	4.48	6.2
G09.86−0.04	18	2.36 <sup>+0.78</sup> <sub>−0.88</sub>	14.39 <sup>+0.87</sup> <sub>−0.78</sub>	2.36	6.0
G10.99−0.09	30	3.31 <sup>+0.69</sup> <sub>−0.76</sub>	13.37 <sup>+0.77</sup> <sub>−0.68</sub>	3.31	6.0
G12.22+0.14	40	3.75 <sup>+0.65</sup> <sub>−0.72</sub>	12.86 <sup>+0.73</sup> <sub>−0.65</sub>	3.75	5.2
G12.50−0.22	36	3.55 <sup>+0.67</sup> <sub>−0.75</sub>	13.05 <sup>+0.75</sup> <sub>−0.67</sub>	3.55	5.2
G14.33−0.57	19	1.99 <sup>+0.85</sup> <sub>−0.95</sub>	14.48 <sup>+0.95</sup> <sub>−0.85</sub>	1.99	2.1
	20	2.04 <sup>+0.85</sup> <sub>−0.94</sub>	14.43 <sup>+0.94</sup> <sub>−0.85</sub>	2.04	
G19.37−0.03	27	2.26 <sup>+0.88</sup> <sub>−0.98</sub>	13.78 <sup>+0.97</sup> <sub>−0.88</sub>	2.26	4.5
G19.40−0.01	27	2.23 <sup>+0.88</sup> <sub>−0.98</sub>	13.81 <sup>+0.97</sup> <sub>−0.89</sub>	2.23	4.5
G23.37−0.29	78	4.70 <sup>+0.90</sup> <sub>−0.88</sub>	10.91 <sup>+0.88</sup> <sub>−0.91</sub>	4.70	9.0
	103	5.69 <sup>+1.20</sup> <sub>−0.91</sub>	9.91 <sup>+0.92</sup> <sub>−1.20</sub>		
G23.48−0.53	65	4.13 <sup>+0.88</sup> <sub>−0.89</sub>	11.47 <sup>+0.90</sup> <sub>−0.87</sub>	4.10	9.0
	64	4.10 <sup>+0.88</sup> <sub>−0.90</sub>	11.50 <sup>+0.89</sup> <sub>−0.89</sub>		
G24.05−0.22	76	4.60 <sup>+0.91</sup> <sub>−0.88</sub>	10.99 <sup>+0.88</sup> <sub>−0.91</sub>	4.82	9.0
	82	4.82 <sup>+0.96</sup> <sub>−0.90</sub>	10.70 <sup>+0.91</sup> <sub>−0.96</sub>		
G24.16+0.08	53	3.46 <sup>+0.91</sup> <sub>−0.94</sub>	12.05 <sup>+0.94</sup> <sub>−0.91</sub>	3.46	9.0
	113	6.13 <sup>+1.03</sup> <sub>−1.23</sub>	9.38 <sup>+0.99</sup> <sub>−1.23</sub>		
G25.99−0.06	90	5.15 <sup>+1.23</sup> <sub>−0.99</sub>	10.13 <sup>+1.23</sup> <sub>−1.23</sub>	5.15	14.0
G30.89+0.14	96	5.65 <sup>+1.38</sup> <sub>−1.14</sub>	8.93 <sup>+1.15</sup> <sub>−1.14</sub>	5.65	8.5
	40	2.62 <sup>+1.14</sup> <sub>−1.15</sub>	11.97 <sup>+1.15</sup> <sub>−1.14</sub>		
G30.98−0.15	108	6.65 <sup>+1.84</sup> <sub>−1.19</sub>	7.94 <sup>+1.19</sup> <sub>−1.62</sub>	4.63	8.5
	78	4.63 <sup>+1.63</sup> <sub>−1.19</sub>	9.94 <sup>+1.19</sup> <sub>−1.62</sub>		
G31.02−0.12	76	4.56 <sup>+1.56</sup> <sub>−1.19</sub>	10.01 <sup>+1.19</sup> <sub>−1.56</sub>	4.56	8.5
	83	4.90 <sup>+1.23</sup> <sub>−1.33</sub>	9.67 <sup>+1.33</sup> <sub>−1.26</sub>		
G32.01+0.05	92	5.41 <sup>+1.33</sup> <sub>−1.51</sub>	9.16 <sup>+1.32</sup> <sub>−1.26</sub>	5.77	8.5
	95	5.77 <sup>+1.51</sup> <sub>−1.26</sub>	8.64 <sup>+1.32</sup> <sub>−1.26</sub>		
G34.63−1.03	14	0.84 <sup>+1.26</sup> <sub>−1.45</sub>	13.14 <sup>+1.32</sup> <sub>−1.26</sub>	3.2	3.7
G34.74−0.12	79	4.86 <sup>+1.45</sup> <sub>−1.26</sub>	9.11 <sup>+1.25</sup> <sub>−1.33</sub>	4.86	
G34.78−0.80	44	2.80 <sup>+1.33</sup> <sub>−1.26</sub>	11.17 <sup>+1.25</sup> <sub>−1.33</sub>	2.80	3.2
	37	2.41 <sup>+1.28</sup> <sub>−1.26</sub>	11.56 <sup>+1.26</sup> <sub>−1.29</sub>		
G35.20−0.72	33	2.17 <sup>+1.29</sup> <sub>−1.28</sub>	11.73 <sup>+1.27</sup> <sub>−1.30</sub>	2.17	3.2
G37.44+0.14	40	2.59 <sup>+1.47</sup> <sub>−1.34</sub>	10.91 <sup>+1.34</sup> <sub>−1.47</sub>	2.59	12.0
	18	1.16 <sup>+1.34</sup> <sub>−1.34</sub>	12.34 <sup>+1.36</sup> <sub>−1.34</sub>		
G37.89−0.15	86	5.90 <sup>+2.12</sup> <sub>−1.35</sub>	7.60 <sup>+1.38</sup> <sub>−1.35</sub>	0.82	12.0
	13	0.82 <sup>+1.35</sup> <sub>−1.51</sub>	12.60 <sup>+1.38</sup> <sub>−1.35</sub>		
	65	4.16 <sup>+1.51</sup> <sub>−2.31</sub>	9.26 <sup>+1.35</sup> <sub>−2.31</sub>		
	86	6.09 <sup>+2.31</sup> <sub>−2.31</sub>	7.33 <sup>+2.31</sup> <sub>−2.31</sub>		

TABLE 4  
MOLECULAR ABUNDANCES AND CLOUD MASSES

Source	Distance <sup>a</sup> (kpc)	N(H <sub>2</sub> ) (10 <sup>21</sup> cm <sup>-2</sup> )	Abundance Relative to H <sub>2</sub>			Cloud Mass	
			N <sub>2</sub> H <sup>+</sup>	C <sup>18</sup> O	CS	(M <sub>☉</sub> ) <sup>b</sup>	(M <sub>☉</sub> ) <sup>c</sup>
G05.85−0.23	3.14	4.4 ± 0.9	2.9E-10	3.5E-7	5.0E-10	2.6E+2	2.5E+2
G06.26−0.51	3.78	13.5 ± 1.2	...	1.3E-7	5.6E-10	...	6.2E+3
G09.16+0.06	3.81	4.4 ± 1.6	...	3.4E-7	4.2E-10	...	3.3E+3
G09.21−0.22	4.57	1.9 ± 1.2	2.0E-9	...	3.2E-9	1.4E+3	...
G09.28−0.15	4.48	7.5 ± 1.2	5.2E-10	...	7.9E-10	3.4E+3	...
G09.86−0.04	2.36	9.8 ± 1.0	9.4E-11	...	7.2E-10	1.5E+3	...
G10.99−0.09	3.32	8.1 ± 0.9	5.5E-10	3.0E-7	5.7E-10	2.0E+3	4.3E+3
G12.22+0.14	3.75	2.8 ± 1.0	1.4E-9	...	3.0E-9	3.2E+2	...
G12.50−0.22	3.55	4.8 ± 1.7	6.5E-10	3.6E-7	1.4E-9	5.4E+2	7.1E+3
G14.33−0.57a	1.99	4.1 ± 0.4	...	5.7E-7	1.4E-9	...	8.3E+2
G14.33−0.57b	2.05	3.4 ± 1.1	4.4E-10	5.7E-7	1.1E-9	1.3E+3	1.2E+3
G19.37−0.03	2.26	2.2 ± 1.5	1.7E-9	...	6.4E-9	2.8E+2	...
G19.40−0.01	2.23	4.9 ± 1.0	2.1E-10	...	7.7E-10	2.1E+3	...
G23.37−0.20	4.70	3.4 ± 1.1	9.0E-10	1.2E-6	3.1E-9	3.3E+3	4.1E+3
G23.48−0.53a	4.10	7.8 ± 3.3	2.0E-10	...	5.4E-10	2.7E+3	...
G23.48−0.53b	4.02	5.7 ± 1.4	2.3E-10	...	6.0E-10	2.0E+3	...
G24.05−0.22	4.82	2.7 ± 1.4	1.1E-9	9.1E-7	1.7E-9	4.0E+2	2.1E+3
G24.16+0.08	3.46	4.0 ± 1.4	...	4.4E-7	...	...	2.6E+3
G25.99−0.06	5.15	4.1 ± 1.5	2.1E-10	...	1.2E-9	6.8E+2	...
G30.89+0.14	5.65	4.2 ± 1.0	3.2E-10	...	6.2E-10	1.1E+4	...
G30.98−0.15	4.63	7.3 ± 2.7	6.6E-10	...	1.4E-9	1.9E+3	...
G31.02−0.12	4.56	4.3 ± 0.9	3.9E-10	3.1E-7	7.1E-10	2.6E+3	4.7E+3
G32.01+0.05	5.77	7.3 ± 2.3	1.0E-9	6.5E-7	2.6E-9	8.7E+3	1.3E+4
G34.63−1.03	0.84	3.6 ± 1.0	3.4E-10	1.7E-7	...	5.5E+1	6.0E+1
G34.74−0.12	4.86	5.1 ± 1.5	4.0E-10	7.3E-7	1.0E-9	8.7E+2	2.4E+3
G34.78−0.80	2.80	6.1 ± 3.8	5.7E-11	3.9E-7	1.4E-9	...	2.9E+3
G35.20−0.72	2.17	3.5 ± 2.5	9.2E-10	6.2E-7	2.5E-9	1.0E+3	1.5E+3
G37.44+0.14a	2.59	3.0 ± 1.5	...	4.0E-7	1.2E-9	...	8.9E+1
G37.44+0.14b	1.16	2.6 ± 0.9	2.6E-10	2.1E-7	4.5E-10	3.2E+1	1.1E+2
G37.89−0.15	0.82	3.2 ± 1.6	1.5E-10	2.1E-7	5.2E-10	3.7E+0	5.4E+1

<sup>a</sup> Distances from rotation curve of Fich, Blitz, & Stark (1989), assuming absorbing cloud lies at near distance.

<sup>b</sup> from N<sub>2</sub>H<sup>+</sup>

<sup>c</sup> from C<sup>18</sup>O

FIG. 1.— The color image is the 8  $\mu\text{m}$  MSX, and the colorbar indicates the emission intensity scale in  $\text{W m}^{-2} \text{sr}^{-1}$ . The contours represent the molecular line integrated intensity, for which the levels are listed for each object. The integrated emission was calculated within a 6 – 10  $\text{km s}^{-1}$  window for  $\text{C}^{18}\text{O}$  and CS. For  $\text{N}_2\text{H}^+$  the window was 15 – 20  $\text{km s}^{-1}$  with some gaps accounting for the clustering of the hyperfine components.

- G05.85–0.23* - blue contours show emission at 17  $\text{km s}^{-1}$ ; green contours: 9  $\text{km s}^{-1}$ . Levels: 1,2 K  $\text{km s}^{-1}$  for all plots.
- G06.26–0.51* - blue contours : 23  $\text{km s}^{-1}$ ; green contours : 17  $\text{km s}^{-1}$ . Levels:  $\text{N}_2\text{H}^+$  : 0.5, 1 K  $\text{km s}^{-1}$ . CS : 1,2,3,4 K  $\text{km s}^{-1}$ .  $\text{C}^{18}\text{O}$  : 1,2,3 K  $\text{km s}^{-1}$  for both velocities.
- G09.16+0.06* - blue contours : 31  $\text{km s}^{-1}$ . Levels:  $\text{N}_2\text{H}^+$  : 1,2 K  $\text{km s}^{-1}$ . CS : 0.5,1,1.5 K  $\text{km s}^{-1}$ .  $\text{C}^{18}\text{O}$  : 1,2,3 K  $\text{km s}^{-1}$ .
- G09.21–0.22* - blue contours : 43  $\text{km s}^{-1}$ . Levels:  $\text{N}_2\text{H}^+$  : 2,4,6,8,10,12 K  $\text{km s}^{-1}$ . CS: 1,2,3 K  $\text{km s}^{-1}$ .
- G09.28–0.15* - blue contours : 42  $\text{km s}^{-1}$ . Levels:  $\text{N}_2\text{H}^+$  : 1.5,3,4.5,6,7.5 K  $\text{km s}^{-1}$ . CS: 0.5,1,1.5,2,3 K  $\text{km s}^{-1}$ .
- G09.86–0.04* - blue contours : 18  $\text{km s}^{-1}$ . Levels:  $\text{N}_2\text{H}^+$  : 1.5,3,4.5,6,7.5 K  $\text{km s}^{-1}$ . CS: 0.5,1,1.5,2,3 K  $\text{km s}^{-1}$ .
- G09.88–0.11* - blue contours : 17  $\text{km s}^{-1}$ . Levels:  $\text{N}_2\text{H}^+$  : 1,2 K  $\text{km s}^{-1}$ . CS: 0.5,1,1.5,2,3 K  $\text{km s}^{-1}$ .
- G10.59–0.31* - blue contours : 17  $\text{km s}^{-1}$ . Levels: 3,5,7,9,11 K  $\text{km s}^{-1}$  for both molecules.
- G10.70–0.33* - blue contours : 0  $\text{km s}^{-1}$ ; green contours : 33  $\text{km s}^{-1}$ . Levels: 2,3,4,5 K  $\text{km s}^{-1}$  for both molecules/velocities.
- G10.99–0.09* - blue contours : 30  $\text{km s}^{-1}$ . Levels:  $\text{N}_2\text{H}^+$  : 2,4,6,8,10 K  $\text{km s}^{-1}$ . CS: 1,1.5,2 K  $\text{km s}^{-1}$ .  $\text{C}^{18}\text{O}$  : 2,3,4,5 K  $\text{km s}^{-1}$ .
- G12.22+0.14* - blue contours : 40  $\text{km s}^{-1}$ . Levels: 1,2,3,4,5 K  $\text{km s}^{-1}$  for each molecule.
- G12.50–0.22* - blue contours : 36  $\text{km s}^{-1}$ . Levels:  $\text{N}_2\text{H}^+$  : 2,4,6,8,10 K  $\text{km s}^{-1}$ . CS: 1,2,3,4 K  $\text{km s}^{-1}$ .  $\text{C}^{18}\text{O}$  : 1,2,3 K  $\text{km s}^{-1}$ .
- G14.33–0.57* - blue contours : 19  $\text{km s}^{-1}$  (solid (a)), 20  $\text{km s}^{-1}$  (dashed (b)) Levels:  $\text{N}_2\text{H}^+$  : 2,4,6,8,10 K  $\text{km s}^{-1}$ . CS : 2,3,4,5,6,7 K  $\text{km s}^{-1}$ .  $\text{C}^{18}\text{O}$  : 4,5,6,7,8,9 K  $\text{km s}^{-1}$  (a); 2,3,4 K  $\text{km s}^{-1}$  (b).
- G19.37–0.03* - blue contours : 27  $\text{km s}^{-1}$ . Levels:  $\text{N}_2\text{H}^+$  : 1,3,5,7,9,11 K  $\text{km s}^{-1}$ . CS : 1,2,5,4,5,5,7 K  $\text{km s}^{-1}$ .
- G19.40–0.01* - blue contours : 27  $\text{km s}^{-1}$ . Levels:  $\text{N}_2\text{H}^+$  : 1,3,5,7,9,11 K  $\text{km s}^{-1}$ . CS : 1,2,5,4,5,5,7 K  $\text{km s}^{-1}$ .
- G23.37–0.29* - blue contours : 78  $\text{km s}^{-1}$ ; green contours : 103  $\text{km s}^{-1}$ ; white contours : 65  $\text{km s}^{-1}$ . Levels:  $\text{N}_2\text{H}^+$  : 3,6,9,12,15,18 K  $\text{km s}^{-1}$  (78  $\text{km s}^{-1}$  component); 4,6,8,10 K  $\text{km s}^{-1}$  (103  $\text{km s}^{-1}$ ). CS : 3,4,5,6,7 K  $\text{km s}^{-1}$  (78  $\text{km s}^{-1}$ ); 3,4,5,6 K  $\text{km s}^{-1}$  (103  $\text{km s}^{-1}$ ); 3,4,5,6,9 K  $\text{km s}^{-1}$  (65  $\text{km s}^{-1}$ ).  $\text{C}^{18}\text{O}$  : 5,7,9,11 K  $\text{km s}^{-1}$  (78  $\text{km s}^{-1}$ ); 3,6,9,12,15,18,21,24 K  $\text{km s}^{-1}$  (103  $\text{km s}^{-1}$ ); 3,6,9 K  $\text{km s}^{-1}$  (65  $\text{km s}^{-1}$ ).
- G23.48–0.53* - blue contours : 64  $\text{km s}^{-1}$ ; green contours : 76  $\text{km s}^{-1}$ . Levels: 1,1.5,2,2.5 K  $\text{km s}^{-1}$  both molecules/velocities.
- G24.05–0.22* - blue contours : 82  $\text{km s}^{-1}$ . Levels:  $\text{N}_2\text{H}^+$  : 1,2,3 K  $\text{km s}^{-1}$ . CS : 1,2,3,4 K  $\text{km s}^{-1}$ .  $\text{C}^{18}\text{O}$  : 1,2,3,4,5 K  $\text{km s}^{-1}$ .
- G24.16+0.08* - blue contours : 53  $\text{km s}^{-1}$ ; green contours : 113  $\text{km s}^{-1}$ . Levels:  $\text{N}_2\text{H}^+$  : 1,2,3 K  $\text{km s}^{-1}$  (113  $\text{km s}^{-1}$  component). CS : 1,2,3 K  $\text{km s}^{-1}$  in both velocities.  $\text{C}^{18}\text{O}$  : 1,2,3 K  $\text{km s}^{-1}$  (53  $\text{km s}^{-1}$ ); 2,4,6 K  $\text{km s}^{-1}$  (113  $\text{km s}^{-1}$ ).
- G25.99–0.06* - blue contours : 90  $\text{km s}^{-1}$ . Levels:  $\text{N}_2\text{H}^+$  : 1,2,3 K  $\text{km s}^{-1}$ . CS : 1,2 K  $\text{km s}^{-1}$ .
- G30.14–0.07* - blue contours : 87  $\text{km s}^{-1}$ . Levels: 0.5 for both molecules.
- G30.53–0.27* - blue contours : 103  $\text{km s}^{-1}$ . Levels:  $\text{N}_2\text{H}^+$  : 0.5 K  $\text{km s}^{-1}$ . CS : 1,1.5,2,2.5 K  $\text{km s}^{-1}$ .
- G30.89+0.14* - blue contours : 96  $\text{km s}^{-1}$ ; green contours : 40  $\text{km s}^{-1}$ ; white contours : 108  $\text{km s}^{-1}$ . Levels:  $\text{N}_2\text{H}^+$  : 2,3,4 K  $\text{km s}^{-1}$  (96  $\text{km s}^{-1}$  component); 2,4,6,8,10 K  $\text{km s}^{-1}$  (40  $\text{km s}^{-1}$ ); 2,4,6,8,10 K  $\text{km s}^{-1}$  (108  $\text{km s}^{-1}$ ). CS : 3,4,5,6,7 K  $\text{km s}^{-1}$  (96  $\text{km s}^{-1}$ ); 2,3,4 K  $\text{km s}^{-1}$  (40  $\text{km s}^{-1}$  and 108  $\text{km s}^{-1}$  components).
- G30.98–0.15* - blue contours : 78  $\text{km s}^{-1}$ . Levels:  $\text{N}_2\text{H}^+$  : 1,2,4,6,8 K  $\text{km s}^{-1}$ . CS : 1,2,3,4 K  $\text{km s}^{-1}$ .
- G31.02–0.12* - blue contours : 76  $\text{km s}^{-1}$ ; green contours : 83  $\text{km s}^{-1}$ ; white contours : 92  $\text{km s}^{-1}$ . Levels:  $\text{N}_2\text{H}^+$  : 1,2,3,4 K  $\text{km s}^{-1}$  (76  $\text{km s}^{-1}$  and 83  $\text{km s}^{-1}$  components); 2,4,6,8,10 K  $\text{km s}^{-1}$  (92  $\text{km s}^{-1}$ ). CS : 1,2,3,4,5,6,7 K  $\text{km s}^{-1}$  (76  $\text{km s}^{-1}$ ); 1,2,3,4,5,6 K  $\text{km s}^{-1}$  (83  $\text{km s}^{-1}$ ); 1,2,3,4,5,6,9 K  $\text{km s}^{-1}$  (92  $\text{km s}^{-1}$ ).  $\text{C}^{18}\text{O}$  : 1,2,3,4,5,6,7,8,9 K  $\text{km s}^{-1}$  (76  $\text{km s}^{-1}$ ); 1,2,3,6,9,12,15,18,21,24 K  $\text{km s}^{-1}$  (83  $\text{km s}^{-1}$ ); 1,2,3 K  $\text{km s}^{-1}$  (92  $\text{km s}^{-1}$ ).
- G32.01+0.05* - blue contours : 95  $\text{km s}^{-1}$ . Levels:  $\text{N}_2\text{H}^+$  : 3,6,9,12,15,18,21,24 K  $\text{km s}^{-1}$ . CS : 2,4,6,8,10 K  $\text{km s}^{-1}$ .  $\text{C}^{18}\text{O}$  : 2,4,6,8,10 K  $\text{km s}^{-1}$ .
- G33.82–0.22* - blue contours : 11  $\text{km s}^{-1}$ . Levels:  $\text{N}_2\text{H}^+$  : 1,2,3 K  $\text{km s}^{-1}$ . CS : 0.5,1 K  $\text{km s}^{-1}$ .
- G34.63–1.03* - blue contours : 14  $\text{km s}^{-1}$ . Levels:  $\text{N}_2\text{H}^+$  : 1,2,3 K  $\text{km s}^{-1}$ . CS : 0.5,1.0 K  $\text{km s}^{-1}$ .  $\text{C}^{18}\text{O}$  : 0.5,1,1.5 K  $\text{km s}^{-1}$ .
- G34.74–0.12* - blue contours : 79  $\text{km s}^{-1}$ . Levels:  $\text{N}_2\text{H}^+$  : 1,2,3 K  $\text{km s}^{-1}$ . CS : 1,2,3,4 K  $\text{km s}^{-1}$ .  $\text{C}^{18}\text{O}$  : 1,2,3,4,5 K  $\text{km s}^{-1}$ .
- G34.78–0.80* - blue contours : 44  $\text{km s}^{-1}$ ; green contours : 37  $\text{km s}^{-1}$ . Levels:  $\text{N}_2\text{H}^+$  : 1,2,3,4 K  $\text{km s}^{-1}$  for both velocities. CS : 1,2,3 K  $\text{km s}^{-1}$  for both velocities.  $\text{C}^{18}\text{O}$  : 1,2,3 K  $\text{km s}^{-1}$  (44  $\text{km s}^{-1}$  component); 1,2,3,4,5,6 K  $\text{km s}^{-1}$  (37  $\text{km s}^{-1}$ ).
- G35.20–0.72* - blue contours : 33  $\text{km s}^{-1}$ . Levels:  $\text{N}_2\text{H}^+$  : 2,4,6,8,10,12,14 K  $\text{km s}^{-1}$ . CS : 2,4,6,8,10,12 K  $\text{km s}^{-1}$ .  $\text{C}^{18}\text{O}$  : 2,4,6,8,10,12,14 K  $\text{km s}^{-1}$ .
- G37.44+0.14* - blue contours : 40  $\text{km s}^{-1}$ ; green contours : 18  $\text{km s}^{-1}$ ; white contours : 86  $\text{km s}^{-1}$ . Levels: 0.5,1,2,3 K  $\text{km s}^{-1}$  for all molecules/velocities.
- G37.89–0.15* - blue contours : 13  $\text{km s}^{-1}$ ; green contours : 65  $\text{km s}^{-1}$ ; white contours : 86  $\text{km s}^{-1}$ . Levels:  $\text{N}_2\text{H}^+$  : 0.5,1,2,3 K  $\text{km s}^{-1}$  (13  $\text{km s}^{-1}$  component). CS : 0.5,1,2,3 K  $\text{km s}^{-1}$  (13  $\text{km s}^{-1}$ ).  $\text{C}^{18}\text{O}$  : 0.5,1,2,3 K  $\text{km s}^{-1}$  (13  $\text{km s}^{-1}$  and 65  $\text{km s}^{-1}$ ); 2,3 K  $\text{km s}^{-1}$  (86  $\text{km s}^{-1}$ ).
- G50.07+0.06* - blue contours 55  $\text{km s}^{-1}$ . Levels: 0.5,1 K  $\text{km s}^{-1}$  for both molecules.

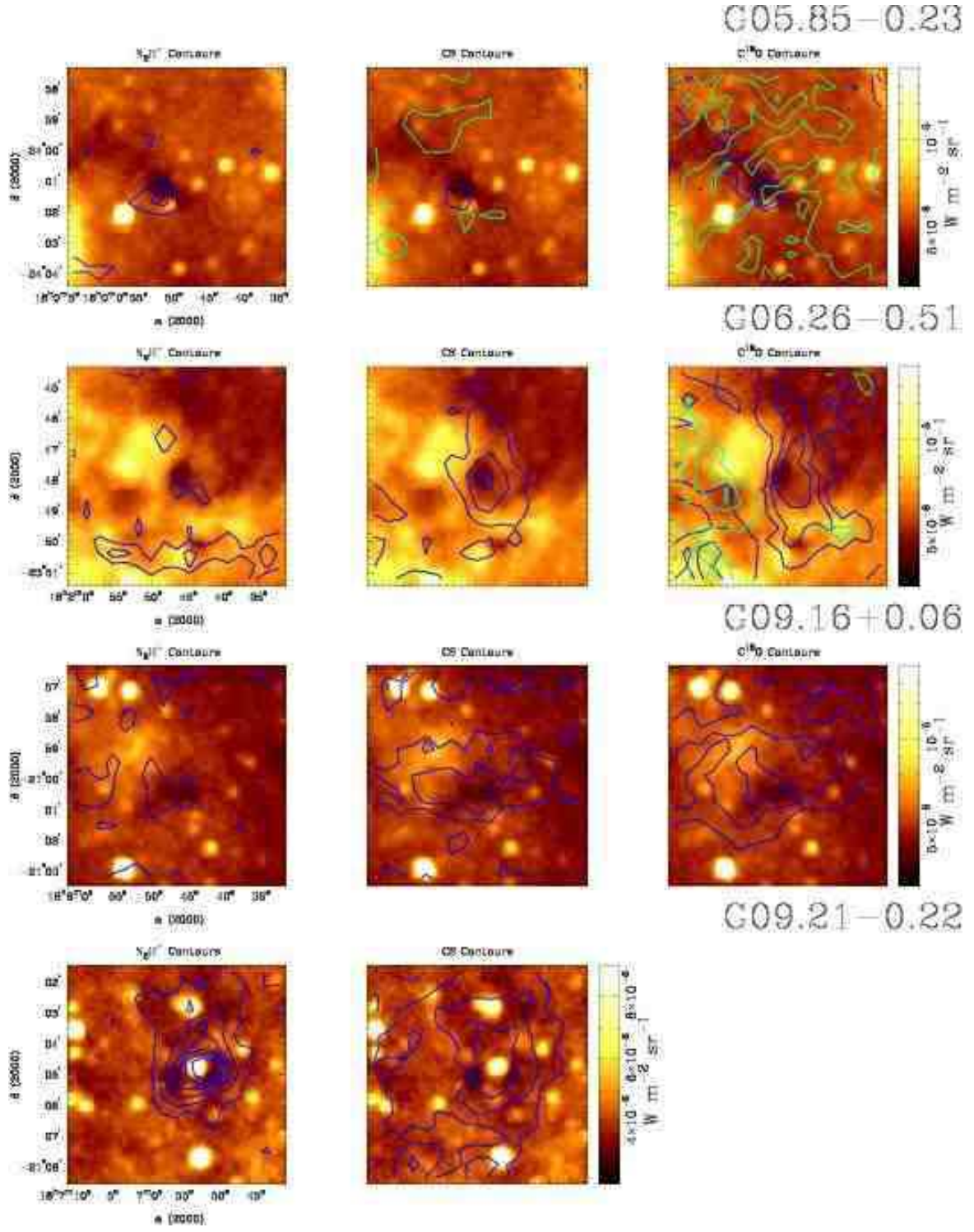


Fig. 1.

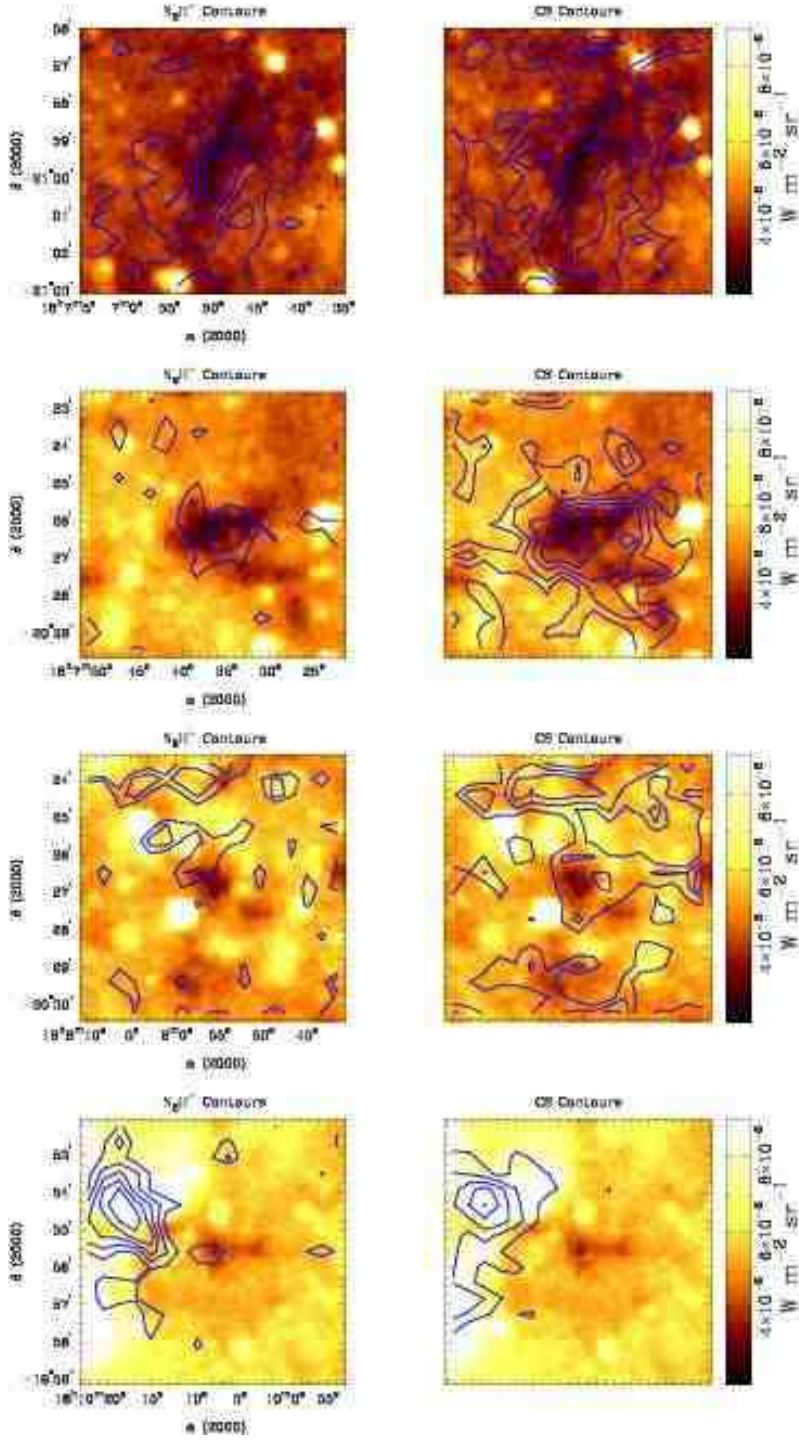


Fig. 1. — Continued

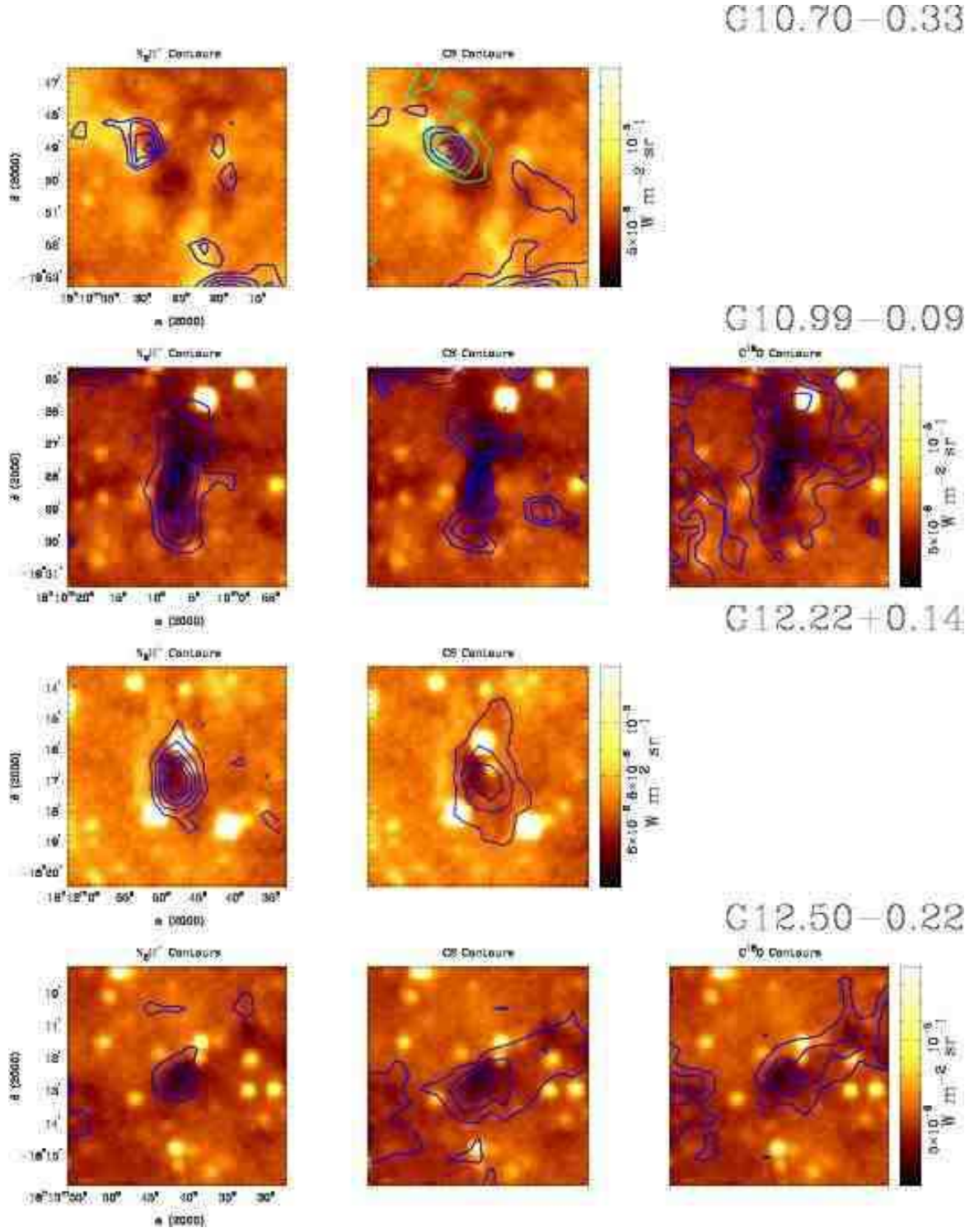


Fig. 1 — Continued

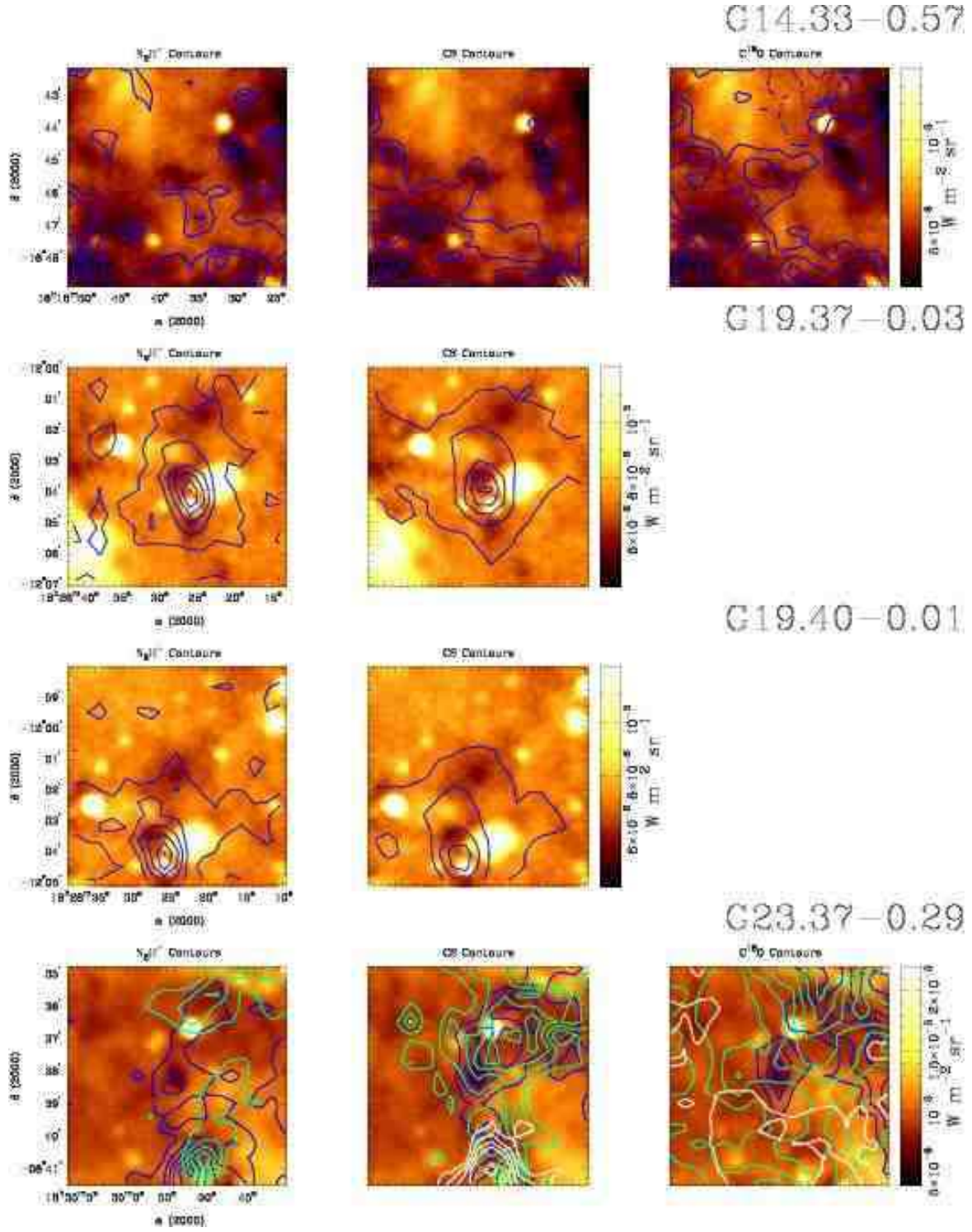


Fig. 1 — Continued

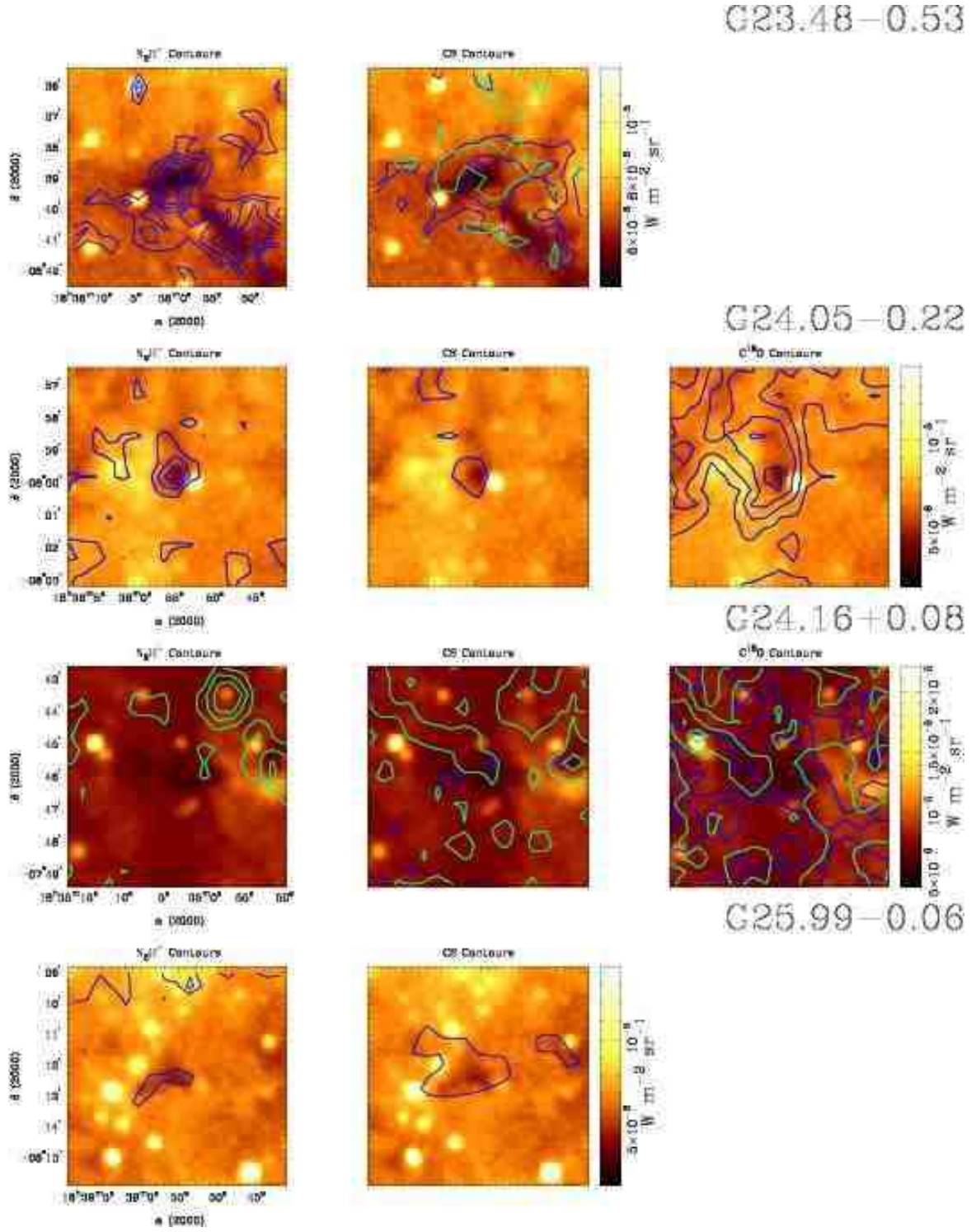


Fig. 1 — Continued

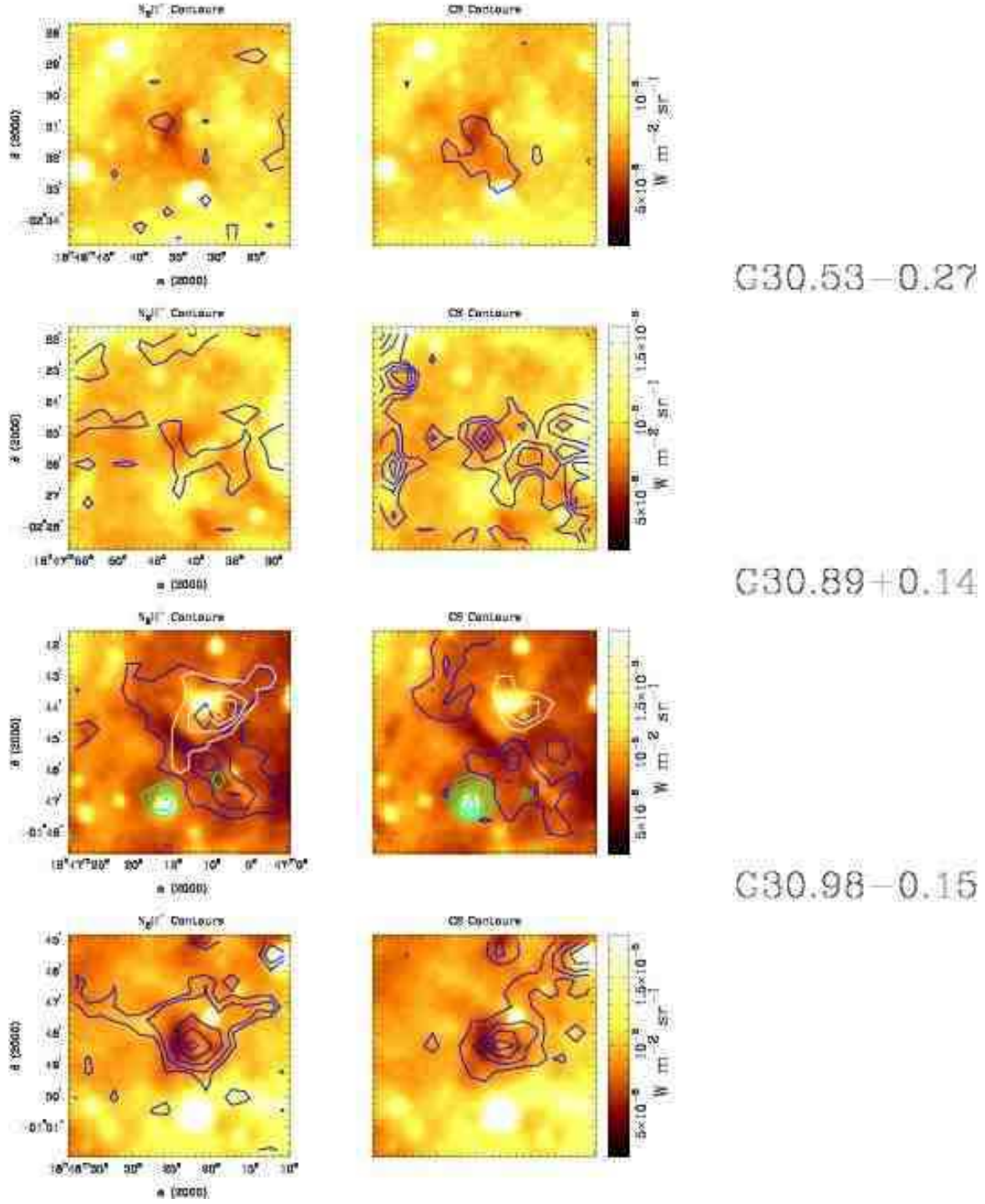


Fig. 1 — Continued

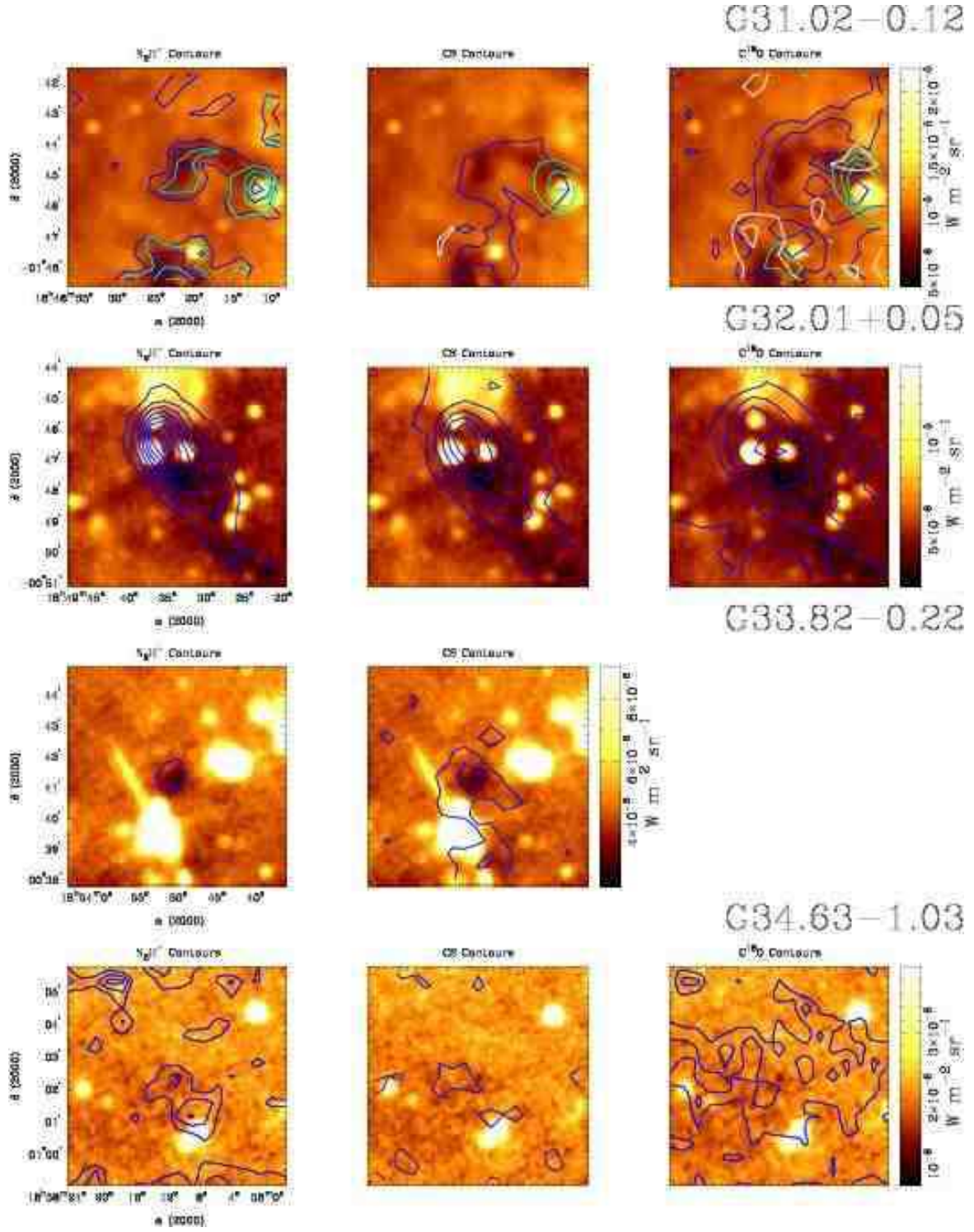


Fig. 1 — Continued

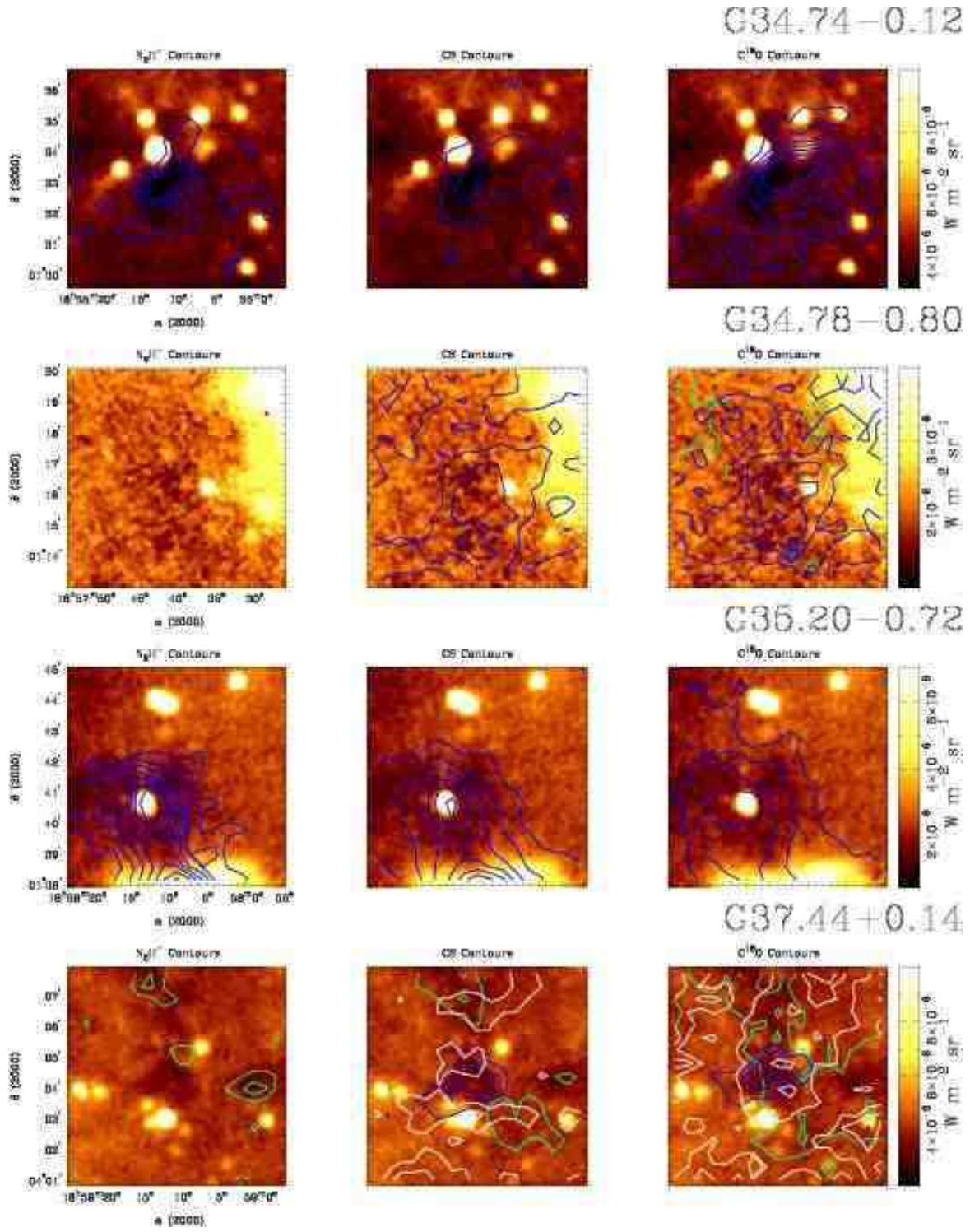


Fig. 1 — Continued

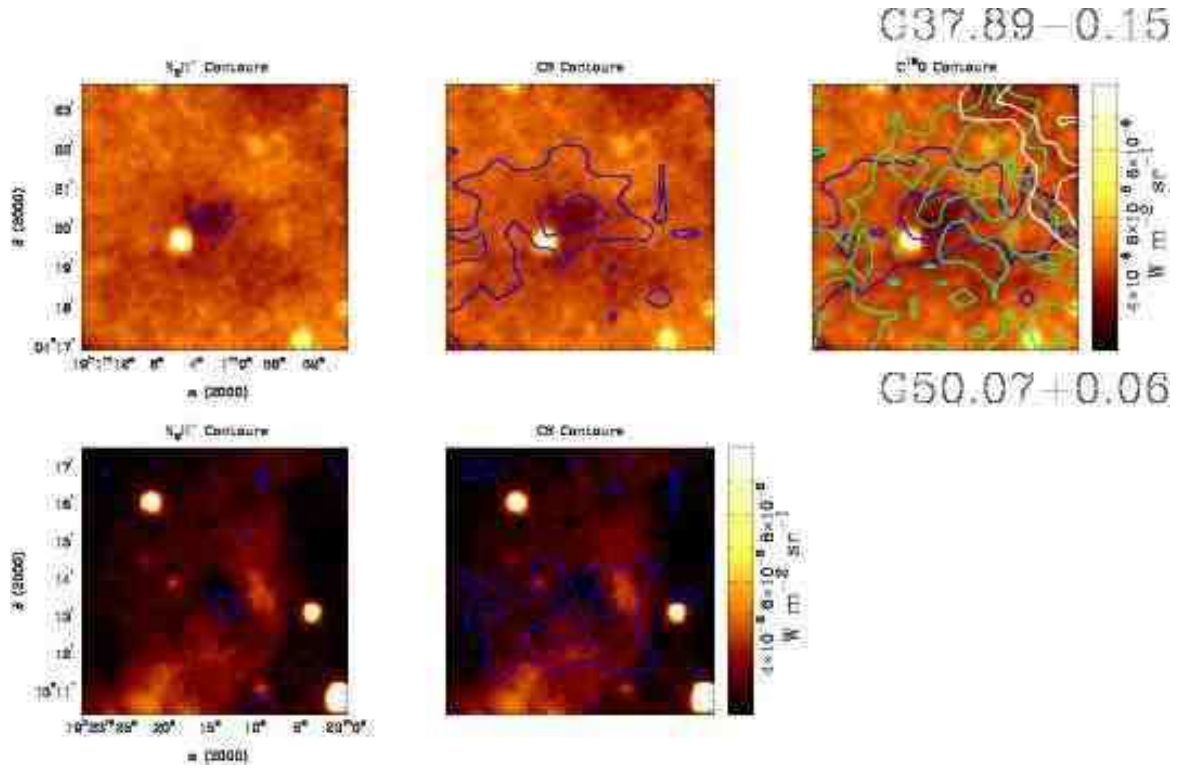


Fig. 1 — Continued

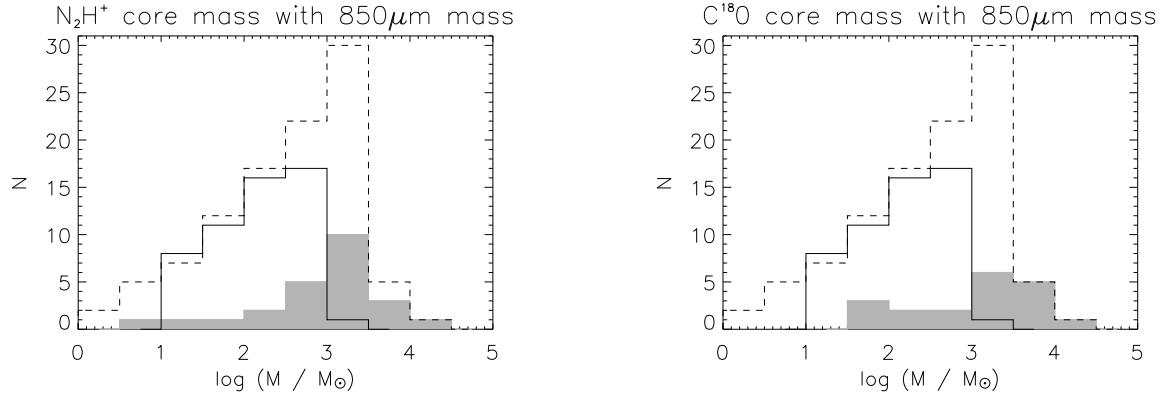


FIG. 2.— Histogram of the mass distribution for our sample of IR dark cores as derived from the  $\text{N}_2\text{H}^+$  data (left panel) and the  $\text{C}^{18}\text{O}$  data (right panel). The grey histograms show the mass distribution for our sample of cores whereas the solid line shows the distribution of masses of the Williams et al. (2004) cores (derived from  $850\mu\text{m}$  data) based on the near galactic distances. The dashed line represents the masses based on the far galactic distances.

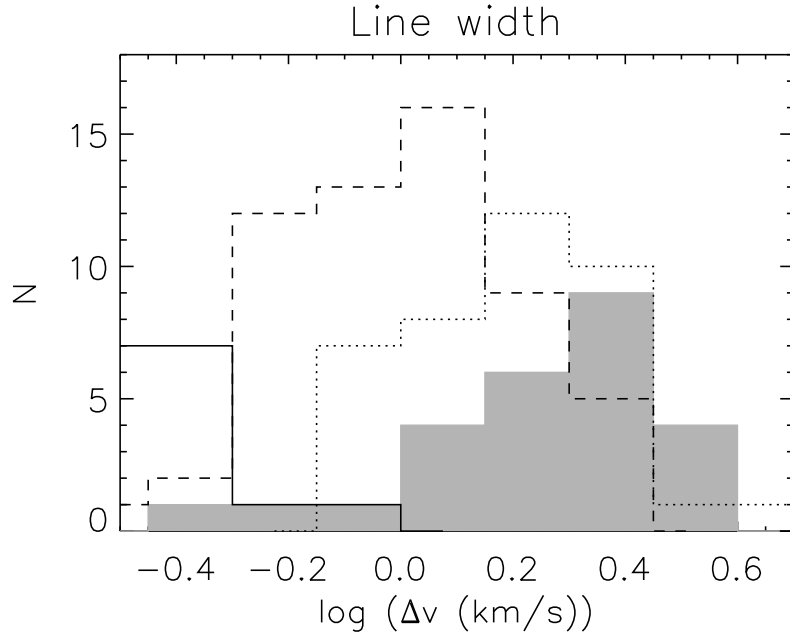


FIG. 3.— Histogram of the  $\text{N}_2\text{H}^+$  (solid line, Caselli et al. 2002; grey, this sample) and  $\text{NH}_3$  (dashed line, Harju et al. 1993; dotted line, Molinari et al. 1996) linewidths.